Emergence of active contractile patterns alters monolayer force generation and transmission in response to focal adhesion distribution

John Robert Davis[1,2‡*], Josephine Solowiej-Wedderburn[3,5,6‡], Sebastián L. Vega[7,8] Jason A. Burdick[9], Carina Dunlop[4,10*], and Nicolas Tapon[1,10*]

[1] Apoptosis and Proliferation Control Laboratory, The Francis Crick Institute, London, UK
[2] Hungry Tissue Lab, Division of Molecular and Cellular Function, School of Biological Sciences, Faculty of Biology Medicine Health, University of Manchester, Manchester, UK
[3] School of Mathematics and Physics, University of Surrey, Guildford, UK
[4] Department of Mathematics, University College London, London, UK
[5] Department of Mathematics and Mathematical Statistics, Umeå University, Umeå, Sweden
[6] Integrated Science Lab, Umeå University, Umeå, Sweden
[7] Department of Biomedical Engineering, Rowan University, Glassboro, NJ, USA
[8] Department of Orthopaedic Surgery, Cooper Medical School of Rowan University, Camden, NJ, USA
[9] BioFrontiers Institute and Department of Chemical and Biological Engineering, College of Engineering and Applied Science, University of Colorado, Boulder, USA
[10] Senior authors
[‡] Authors contributed equally
[*] Correspondence: john-robert.davis@manchester.ac.uk (JRD), carina.dunlop@ucl.ac.uk (CD), and nic.tapon@crick.ac.uk (NT)

Abstract

For tissue development, cells must generate contractile forces which are transmitted to their surrounding matrix or neighbouring cells via adhesion complexes. It is often envisaged that a simple linear counterbalance of cell generated stress with extracellular matrix (ECM) traction forces exists. However, experimental evidence indicates that modulating cell-ECM attachment does not necessarily lead to expected reciprocal changes in intercellular stresses. As ECM composition or mechanical properties are rarely uniform, it is important to understand the complexity of how focal adhesions alter stress transmission and the force-balance of a tissue. To address this, we confined monolayers on adhesive patterns altering focal adhesion distribution. Traction force microscopy and laser ablations of cell-cell junctions were used to examine stresses across epithelial monolayers whilst modulating substrate stiffness. We show that monolayers reach different force-balance states depending on focal adhesion distribution. Using an active matter model and confirmed experimentally, we reveal that a force-balance is generated by non-uniform patterns of cell contractility linked to adhesion patterning. This work highlights the importance of integrating the position of cell-ECM attachments into our vision of the mechanical landscape of living tissues.

Teaser

To infer a tissue's force-balance, positional information of focal adhesion distribution needs to be integrated due to the emergence of non-uniform patterns of cell contractility.

53 **Introduction**

54 A key aspect of many developmental, physiological, and pathological processes is the
55 ability of cells to generate and transmit forces across a tissue. Cells transmit intracellular
56 stresses to their environment, and this is essential for orchestrating cooperative behaviours
57 such as morphogenesis[1], collective migration[2] and wound healing[3]. Stresses are transmitted
58 through adhesion complexes[4]; either to the substrate generating traction stresses, or to
59 neighbouring cells generating intercellular stresses. Furthermore, these adhesion complexes
60 are important mechanotransduction nodes regulating cellular processes such as
61 metabolism[5], gene transcription[6], as well as actin architecture[7]. Therefore, to gain biological
62 insight linking tissue mechanics to molecular dynamics, there is a need to quantify local
63 traction stresses and intercellular stresses across epithelial monolayers.

64 Various methodologies are available to interrogate stresses within tissues[8]. Traction
65 force microscopy, where the movement of microbeads embedded within a substrate are
66 tracked, is a proven method for examining cell-generated forces transmitted to the
67 substrate[9]. As a fundamental principle of tissue mechanics is the necessity for monolayers
68 to balance traction and intercellular stresses to maintain epithelial integrity traction force
69 microscopy has been extended to infer intercellular stresses based on mechanical
70 arguments [10–14]. This has been developed for a range of scenarios from cell doublets[14–17], to
71 small cell clusters[13] to entire epithelial sheets[10,12,18,19]. A core assumption of these
72 techniques is that intercellular stresses can be inferred from traction stresses through a
73 passive elastic model, often diagrammatically evoked as a tug-of-war stalemate. This type of
74 model leads to two conclusions: 1) that there is a linear relationship between the scalar sum
75 of traction stresses and intercellular stresses within a monolayer[13,14], and 2) that
76 intercellular stress would be greatest in the centre of the monolayer and lowest at the
77 boundary[20,21]. There are some experimental data based on Förster resonance energy
78 transfer (FRET) tension sensors which support these conclusions. Both E-Cadherin and ZO-2
79 tension sensors have been reported to decrease in FRET efficiency (increase in molecular
80 tension) in monolayers cultured on stiffer substrates[22,23]. Furthermore, E-Cadherin-α-
81 catenin tension sensors have also been reported to exhibit a reduction in FRET efficiency
82 away from the edge of a wounded epithelium[24]. However, it has also been reported in cell
83 doublets that cell-cell forces inferred from traction force data do not correlate with the
84 FRET-efficiency of an E-Cadherin tension sensor, with the authors proposing a molecular

tension homeostasis mechanism to resolve these findings[16]. Furthermore, experiments examining intercellular stresses through laser ablation have also made observations which are not consistent with the conclusions drawn from passive elastic models linking traction stresses and intercellular stresses.

Laser ablation is a widely employed technique to quantify intercellular stresses within tissues and through rheological models infer tissue mechanical properties. This is achieved by examining the relaxation of cells after individual or groups of junctions have been cut[25,26]. By disrupting entire cell-cell junctions, this method provides a holistic overview of cell mechanics incorporating both cortical cytoskeleton and all cell-cell adhesion complexes. It is widely used in developmental systems that are not amenable to other types of biomechanical techniques to measure or infer tissue mechanics but is also applied to cells *in vitro* to examine both intracellular and intercellular stresses. Work in the *Drosophila* abdominal epidermis showed that degradation of the basal ECM occurring at the pupal stage led to an increase in intercellular tension[27]. Similarly, Madin-Darby canine kidney (MDCK) cells cultured on large micropatterned disks on soft hydrogels showed lower traction stresses but higher recoil velocities than those cultured on stiff hydrogels [28]. These contradict the conclusions drawn from passive elastic models employed to link traction stresses to intercellular stresses. In both studies, intercellular tension was greatest when cell-ECM friction was reduced, in the case of *Drosophila* abdomen the ECM was degraded [27] and for MDCK cells there was weaker cell-ECM attachments on softer hydrogels[28] which leads to a reduction in cell-ECM friction[29]. This supports pioneering work in amnioserosa cells during *Drosophila* embryonic dorsal closure showing that focal adhesions act as tethers that reduce both intercellular tension and stress transmission[30]. Taken together, these studies question the use of simple passive elastic models to infer intercellular stresses from traction stress which do not explicitly model the active cell contractile behaviours, leading to proposals to replace these types of models with active-matter models[31]. This approach directly accounts for active contractility within the force balance enabling both active cell-generated stress and the material stress generated in passive cell structures to be decoupled, and this approach is now widely adopted in a range of contexts[32–37]. The benefit of the active matter framework is that it is highly adaptable and capable of capturing a range of the complexity in the cell-ECM force balance including ECM stiffness-induced changes. Significantly, cell adhesions and adhesion patterning can be explicitly

117 described[38,39], which is significant given recent experimental findings that highlight that 1)
118 the distribution of focal adhesions is important in determining the length-scale that stresses
119 can be transmitted through the monolayer[30], and 2) that the compliance of the substrate
120 also influences the distance stresses can be transmitted through the substrate[40]. Indeed, it
121 is intuitively clear that examining the relationship between intercellular and traction
122 stresses across a monolayer requires an understanding of how both focal adhesion
123 distribution and substrate compliance alter the acquired force-balance. This is especially
124 true when considering that *in vivo* ECM composition, architecture and mechanical
125 properties are often heterogeneous[41].
126 To examine the relationship between traction and intercellular stresses we
127 combined traction force microscopy and annular laser ablation[25]. As traction forces are
128 known to be dependent on the size and geometry[34,38] of cells and tissues, we employed
129 micropatterning of hydrogels to standardise these factors. Furthermore, through
130 micropatterning we modulated cell-ECM interactions by culturing monolayers on disks or
131 rings to examine the role of focal adhesion distribution in determining monolayers
132 mechanical equilibrium. We also modulated substrate compliance which is known to alter
133 both substrate stress transmission[40] and traction stresses generated by cells[38]. When focal
134 adhesions are distributed throughout the monolayer, traction forces are dependent on the
135 substrate stiffness within our experimentally tested range. However, when focal adhesion
136 distribution is mainly restricted to the periphery, traction forces become independent of the
137 substrate. Furthermore, we observe that intercellular stress is inversely proportional to
138 substrate stiffness, so that intercellular stress reduces as hydrogel stiffness increases. We
139 combined this experimental approach with an active stress model based on a continuum
140 description, which explicitly modelled cell attachments and variation of cell activity within
141 the layer. This revealed that the relationship between substrate stiffness and intercellular
142 stress is elicited by the emergence of non-uniform contractility across the monolayer, with
143 greater contractility present at regions with greater adhesions.
144

145 **Results**

146

147 Adhesive surface area dictates focal adhesion distribution across a monolayer

148 To examine the relationship between traction and intercellular stresses, we cultured
149 non-tumorigenic mouse mammary epithelial cells (EpH4)[42] on methacrylated hyaluronic
150 acid (MeHA) hydrogels[43]. 3% w/v MeHA solutions were crosslinked with a range of
151 dithiothreitol (DTT) crosslinker concentrations to modulate the rigidity of hydrogels from
152 10.8 ± 2.5 kPa to 31.4 ± 2.8 kPa at intervals of ~5kPa (Fig. S1a-c). Whilst these values are
153 higher than what has been reported for mouse mammary tissue[44], they span reported
154 basement membrane values[41] and ranges employed in other systems examining stress
155 transmission[14,28,29,40]. To examine the role of focal adhesions in determining monolayers
156 mechanical equilibria, we modulated the adhesive surface area beneath monolayers by
157 micropatterning laminin, EpH4 cell's preferred ECM component[45]. MeHA hydrogels were
158 patterned with either disk (Fig. 1a) or ring (Fig. 1b) micropatterns, with an outer diameter of
159 200μm (approximately 10 – 20 cells wide) and the width of rings being 20μm
160 (approximately 1-2 cells wide). We conjugated an Alexa633 fluorophore to laminin to assess
161 if increasing levels of MeHA crosslinking increased the concentration of laminin on the
162 surface of hydrogels for both disk (Fig. 1c) and ring (Fig. 1d) patterns. Whilst there were
163 fluctuations in laminin intensity on different hydrogel stiffnesses (Fig. 1c,d) these did not
164 follow a particular pattern linked to substrate stiffness. Furthermore, whilst there were
165 radial differences across the disk pattern (Fig. 1c), these did not correlate with differences in
166 focal adhesions (Fig. 1g). Therefore, the concentration of laminin in patterned areas appears
167 to not alter the adhesions that cells can generate with the substrate.

168 To measure active focal adhesions on different patterns, we immunostained
169 monolayers for phosphorylated focal adhesion kinase (pFAK) (Fig. 1e,f) as previously
170 reported [add Pere paper]. Altering the adhesive surface did lead to changes in the
171 distribution of pFAK across the monolayer. On disks, pFAK was evenly distributed across the
172 entire monolayer with a slight peak at the periphery (Fig. 1g). On rings however, pFAK was
173 mainly focused on the perimeter of the adhesive area with peaks at the boundaries, and a
174 low-level present in the non-patterned area (Fig. 1h). As no laminin is present in the middle
175 of the ring micropatterns (Fig. 1d), the low-level of pFAK staining in this region is probably
176 due to nascent proteins secreted by EpH4 cells becoming bound to the substrate[46,47] and

177 not direct binding to the MeHA gel. Indeed, our hyaluronic modification rate was between
178 76 – 79% (Fig. S1a), far higher than the threshold for cells to bind to unmodified
179 disaccharides[48]. Furthermore, whilst cells cultured on disks were surrounded by pFAK
180 puncta (Fig. 1e) across the monolayer, on rings, cells in the centre tended to only have
181 isolated puncta of pFAK (Fig. 1f). Examining the total pFAK coverage beneath disks and rings
182 revealed that rings consistently had less total pFAK coverage than disks (Fig. S1d,e),
183 suggesting that monolayers cultured on ring micropatterns had reduced active cell-ECM
184 attachments. Surprisingly, given previous reports[29] both patterns showed a slight reduction
185 in total pFAK as substrate stiffness increased (Fig. S1d,e). The regulation of focal adhesion
186 dynamics is dependent on many factors[49], and there are contradictory reports on how
187 substrate rigidity alters focal adhesion coverage[50,51]. It is not clear why total pFAK coverage
188 reduces on stiffer hydrogels, however, cells have been reported to sense and respond to
189 strain energy[52], and as we are examining active focal adhesions it is possible that strain
190 energy is decreasing as stiffness increases in EpH4 cells across the range of rigidities
191 employed. In summary, we established experimental conditions that allow us to vary cell-
192 ECM adhesion distribution and substrate stiffness.
193 We next examined if altering the adhesive pattern or substrate rigidity altered cell-
194 cell adhesions or cell morphology across the monolayer. We observed no obvious
195 differences in the localisation of E-Cadherin for both patterns on all hydrogel stiffnesses,
196 with strong localisation along entire cell boundaries (Fig. 1e,f). Likewise, whilst there was a
197 distribution in the number of cells that composed each monolayer, the distribution was
198 similar for all patterns and substrate rigidities (Fig. 1i,j). Examining cell morphology, we
199 observed that cell height does not significantly change as substrate rigidity increases (Fig.
200 1k,l). However, we did observe that whilst on disks height is relatively constant (8.9 ±
201 1.3μm; Fig. 1k), on rings height increases from 8.9 ± 1.8μm in the centre to 10.4 ± 1.8μm on
202 the adhesive area (Fig. 1l). Cell area tended to be slightly greater in the centre of the
203 patterns, especially for disks (Fig. S1f,g) and there tended to be a slight increase in
204 elongation at the perimeter for both patterns (Fig. S1h,i). However, these variations were
205 subtle between the different patterns suggesting that overall monolayer packing was similar
206 between patterns and on all substrate stiffnesses.
207 Finally, we examined whether there were junctional rearrangements over the
208 timescale of our movies. In our timelapse experiments, we imaged for one minute before

209 performing laser ablations, so subtracted the frame prior to laser ablation from the initial
210 frame and calculated the percentage pixel intensity of our membrane label that remained.
211 This analysis revealed a value close to zero on both patterns and on all hydrogel stiffnesses
212 (Fig. S1j,k). Furthermore, overlayed images of cell membranes for the same duration as our
213 ablation experiments (5 minutes apart), showed a high degree of overlap (Fig. S1l). We
214 therefore assume that junctional rearrangement is not a major contributing factor to the
215 force balance dynamics of the monolayer at the timescale of our experiments.
216
217 Focal adhesion patterning alters dependence of traction forces on substrate stiffness
218 We next wanted to assess how altering the adhesive area affected traction forces. To
219 measure traction forces, we embedded fluorescent microbeads within the MeHA hydrogels
220 and measured their displacement[53]. Following recent reporting of extensile forces
221 generated by MDCK cell layers[28], we first confirmed that all displacement vectors indicated
222 contraction towards the centre of the cell layer across all substrates (Fig. 2a,b, Fig. S2a-d).
223 We also observed the greatest displacements at the periphery of the monolayer (Fig. 2a,b,
224 Fig. S2e,f). As expected from previous reports[28,38], we observed a reduction in displacement
225 magnitude as substrate rigidity increased for both disks and rings (Fig. 2c,d, Fig. S2g-h). We
226 next examined the traction forces generated by the monolayers and noticed stark
227 differences between disk and ring patterns (Fig. 2e-h). On disk patterns we observe a
228 decrease in both the scalar sum of traction forces, which we term total traction, and the
229 maximum traction force as substrate stiffness increased (Fig. 2e,g). On rings, total traction
230 force remained almost constant (Fig. 2f), and maximum traction forces showed a weak
231 reduction (Fig. 2h). It has been reported in micropatterned single MDCK cells that strain
232 energy is not affected by substrate rigidity[38]. In the case of the monolayers considered here,
233 as displacement decreased for both patterns and traction forces decreased on disks and
234 remained constant on rings, we were interested in examining if our adhesive patterns
235 showed marked differences in strain energy. We observed that for both disks and rings
236 there is a decrease in strain energy as substrate stiffness increases, potentially explaining
237 the reduction in pFAK. However, this difference is stronger for disks than it is for rings (Fig.
238 2i,j), with a mean strain energy reduction between 10kPa to 30kPa for disks (25,242pJ)
239 being almost double that of rings (13,481pJ).

240 As the traction forces highlighted a clear difference in behaviour between disk and
241 rings on different substrates, we decided to examine whether this reflected a difference in
242 the spatial distribution of traction forces. Examining mean traction forces radially along the
243 epithelial clusters showed the highest traction forces at the periphery for both ring and disk
244 patterns on all substrates (Fig. 2k,l). Consistent with changes in total and maximum traction
245 forces, for disks we observe a reduction in traction magnitude with increasing stiffness
246 whilst on rings we observe virtually no change in traction force magnitude (Fig. 2k,l).
247 However, we noticed a slight change in the distribution of traction forces radially between
248 the patterns, with traction forces appearing to be more localised at the periphery on rings
249 than in disks especially on soft substrates (Fig. 2k,l). As our pFAK data shows on disks all cells
250 are surrounded by focal adhesions, this suggests that on compliant substrate, cells within
251 the monolayer locally contribute towards deforming the substrate, leading to a gradual
252 radial accumulation in traction forces. However, as the hydrogel becomes more rigid and
253 cells are less able to deform the substrate, traction forces become more localised to the
254 edge, as previously theoretically predicted[54]. This is altered on ring patterns where the cells
255 in the central non-adhesive region do not deform the substrate locally, so that the applied
256 traction forces are always localised to the periphery. Taken together our results suggest that
257 altering the adhesive surface leads to changes in the generation and distribution of traction
258 forces across the epithelium.
259
260 Intercellular stresses decrease with increasing substrate stiffness
261 To interrogate stress transmission within the monolayer, we combined theoretical
262 and experimental approaches. The theoretical model specifically describes the monolayer as
263 an active soft material in which the monolayer stresses and displacements are determined
264 from continuum elasticity theory; specifically, we include an isotropic active stress in the
265 relationship between stress and strain that accounts for the cell-derived contractility (Fig.
266 3a, see Supplemental Information Table 1 for model parameters) in contrast to passive
267 models for traction-force inference. Such active matter models are widely adopted to
268 describe active, contractile cells and tissues adhered to substrates[17,35,38,54]. Within our
269 framework, substrate adhesion is coupled into the active model in the force balance
270 equations through applied tractions, which may be restricted (as here) to act only where the
271 layer is adhered[54]. Based on our experimental observations with pFAK staining (Fig. 1i,j),

272 layers were either modelled as adhered uniformly to recapitulate the disk, or for the ring
273 pattern the model assumes adhesions concentrated at the ring but with an accompanying
274 underlying distribution of small adhesions sites everywhere else as observed (Fig. 3a). A
275 more detailed description of the model can be found in supplemental information and
276 methods section.

277 As we observe a reduction in total adhesion coverage as substrate stiffness increases
278 (Fig. S1d,e), we examined in our model the sensitivity of total traction forces to different
279 levels of adhesion coverage (Supplemental Information). This revealed that traction forces
280 remained relatively constant with different total levels of adhesion coverage above a 10%
281 coverage threshold (Supplemental Information Table 2). As the coverage of adhesions is
282 greater than 10% for all our conditions, we conclude that the reduction in adhesion
283 coverage we observe does not drastically limit the traction stresses generated by the
284 monolayer. Indeed, this analysis also shows that our results are insensitive to exact details
285 of the underlying distribution of adhesions distributed throughout the layer. As the
286 monolayer was stable at the timescales measured (Fig. S1k-m), we considered the system to
287 be in a stationary steady state and the forces balanced. The model can be used to fit both
288 the displacement data (Fig. 3b,c) and total traction (Fig. 3d,e) for each substrate stiffness,
289 with the cell-generated contractile stress as the fit parameter. In fitting this data, we
290 assume uniform contractility across the layer so that each cell is equally mechanically active.
291 Where active matter models are used to describe traction force-type experimental systems
292 the assumption of constant contractility is common[31–34,55]. Assuming that each cell across
293 the layer had the same uniform contractility was sufficient to reproduce the observed
294 traction force microscopy data, with small variations in this overall contractile activity on
295 each stiffness. As with monolayer stress inference techniques, we then extended this
296 analysis of traction forces to infer internal stress within the layer, akin to intercellular stress,
297 which can be determined from the force balance equations. As a reference point, we plot
298 the internal radial stress halfway across the radius (r=50μm; Fig. 3f,g). As might be
299 intuitively expected, the model predicts internal stresses that broadly follow the same
300 qualitative trends observed for total traction across both disks and rings. For the disks, we
301 predict a significant monotonic decrease as substrate stiffness increases, with the greatest
302 stresses being on the softer substrates (Fig. 3f). Whilst for the ring patterns, we see that the
303 stress remains broadly constant across the stiffnesses (Fig. 3g). We next sought to examine

304 experimentally whether the model's internal stress predictions were accurate by
305 considering both traction stresses using traction force microscopy and intercellular stresses
306 inferred from laser ablation.
307 We bisected the epithelial monolayers with an annular region of interest (ROI) (Fig.
308 3h) to infer bulk intercellular stresses[25], and analysed the recoil velocity (Fig. S3a,b). We
309 observed that the greatest recoil was near the ablation site, and that vectors were
310 orientated away from the cut highlighting that the monolayers were always under tension
311 (Fig. 3i,j, Fig. S3c-f). Measuring the maximum recoil velocity half-life revealed a similar
312 relaxation time of ~20 $\pm$ 10s for both patterns and all stiffnesses. Assuming that the cells'
313 Young's modulus is independent of substrate stiffness as previously reported[56], this suggests
314 that the viscoelastic properties of the monolayer were not altered by focal adhesion
315 patterning or substrate stiffness (Fig. S3g-j). We then examined the maximum recoil velocity
316 with respect to substrate stiffness for both patterns. For the disk pattern, the recoil velocity
317 showed a weak decrease (Fig. 3k) qualitatively similar to the model prediction, but with the
318 reduction in internal stress being more subtle than that predicted (Fig. 3m). On ring
319 patterns, while the model predicts a constant recoil velocity, we observed a consistent
320 decrease with increasing stiffness (Fig. 3l). This reduction, which is not intuitively expected
321 or predicted by the model, suggests that a model with uniform mechanical activity does not
322 describe the system fully and that additional factors must be at play.
323 Comparing traction forces before and after ablation also revealed a reduction,
324 highlighting mechanical coupling of stresses within the monolayer to the tractions applied
325 to the substrate (Fig3o,p). Extending this analysis to the strain energy, we also observed a
326 reduction in strain energy after ablation on both patterns (Fig. 3q,r), with the exception for
327 disks on the stiffest hydrogel where differences were negligible (Fig. 3q). As total traction
328 and strain energy vary for the different patterns and substrate stiffnesses, we examined the
329 percentage change to assess whether this reduction merely reflected the loss of cells in the
330 ablation region (Fig. 3o'-r'). This revealed that the percentage loss of traction forces and
331 strain energy (Fig. 3o'-r'), tended to be higher for rings than for disks. Taken together, this
332 supports the assumption that there is stress transmission from cell-cell interactions which
333 distributes forces into the substrate, and releasing intercellular stress through ablation leads
334 to a reduction in traction stresses generated by the monolayer.
335

336 Theoretical modelling suggests non-uniformity of contractility

337 To illustrate the incompatibility of a model with uniform contractility, where all cells
338 generate equal active forces across the monolayer, with the observed recoil velocities we
339 focused on the ring pattern which experimentally shows a constant total traction of
340 ~53.7MPa (Fig. 2f) but a reduction in recoil velocity as substrate stiffness increased (Fig. 3l).
341 For uniform contractility (Fig. 4a) we used our model to examine how the constant
342 contractility (P=a) would have to be altered to maintain a constant internal stress
343 (represented in blue) or constant total traction force (represented in red) as substrate
344 stiffness increased. To orientate, we plotted an illustrative contour of constant internal
345 stress at r=0.5 (which corresponds to the ablation region, blue line) this enables us to
346 identify a region below the contour (shaded in blue) which has a lower internal stress at
347 r=0.5 (blue shaded region, Fig. 4a) as required. Likewise, we also plotted an illustrative
348 contour of constant total traction (red line) and shaded the region above the contour which
349 has greater traction forces (red shaded region, Fig. 4a). Note that with uniform contractility
350 the shaded regions do not generate a practically relevant overlap (Fig. 4a), so that we
351 cannot attain lower internal stress with constant traction, and a parameter sweep altering
352 the contractility of the layer demonstrates that this is true for all physically relevant regimes
353 (Supplemental information). This highlights that, as the system maintains a constant
354 traction force (red contour) it does not encroach into the lower internal stress regime (blue
355 shaded region). This would inevitably lead to a system whereby changes in traction forces
356 would lead to similar changes in internal stress as previously predicted by monolayer stress
357 inference techniques based on passive elastic models (Fig. 3f,g,[10,13,14,18]).

358 These phase plane plots do suggest a potential resolution by considering a non-
359 uniform distribution of mechanical contractility within the layer. By increasing contractility
360 at the edges, the system generates an overlap region where it is possible to maintain total
361 tractions but reduce internal stress (Fig. 4b). In the examples given, to maintain a constant
362 internal stress within the layer (blue line) traction forces must increase as the blue contour
363 now encroaches the shaded orange region, and similarly to maintain constant total traction
364 forces (red line) the internal stress must decrease as it now encroaches the blue shaded
365 region (Fig. 4b). As the latter example is similar to our experimental observations, we
366 explored whether parameterising the mechanical gradient could reconcile theoretical
367 predictions with experimental observations.

368 We introduced a new contractility function that generates monotonic increasing
369 contractility. Specifically, we take $P(r) = a(1 + br^5)$, as this enables analytical solutions in
370 restricted cases and simplifies the numerical solution (see Supplemental Information). Here
371 increasing b indicates more concentrated contractile activity at the edge (b=0 returns the
372 model to uniform cell contraction). By parameterising the total contractility (P_{Total}) of the
373 monolayer and distribution of contractility (b), we were able to fit both tractions and
374 relative changes in internal stress across the range of stiffnesses for both disk (Fig. 4c) and
375 ring patterns (Fig. 4h). Namely we find that the model can reproduce a large decrease in
376 traction and slight decrease in internal layer stress on disk patterns with increasing stiffness
377 (Fig. 4d-f), while also reproducing nearly constant total tractions and large decrease in
378 internal layer stress on the ring pattern as stiffness increases (Fig. 4i-k). Looking beyond the
379 cell traction and recoil data, we considered the strain energy of the system. Non-uniform
380 contractility within the model also reproduces the trends observed in the strain energy of
381 both adhesive patterns (Fig. 4g,l), successfully capturing the observed reduction in strain
382 energy for disks (Fig. 4g) but only qualitatively for ring patterns (Fig. 4l). However,
383 considering that ring patterns have lower adhesion coverage than disks, a deviation in strain
384 energy may be expected given the linear model of substrate resistance to deformation and
385 the contribution of non-local effects from the thickness of the hydrogel (see Supplementary
386 Information). Taken together, introducing non-uniform contractility into the model can
387 recapitulate experimental observations.
388 Significantly, we find a qualitative difference in behaviour between disk and ring
389 patterns for resolving experimental observations. For disk patterns the contractility must
390 become more uniformly distributed, with more cells sharing the work as stiffness increases
391 (Fig. 5a). However, on the ring pattern the opposite trend is required, with cells at the edge
392 of the layer being required to be more contractile compared with the rest of the layer as
393 stiffness increases, so that these edge cells do much of the work (Fig. 5a).
394
395 <u>Active myosin and F-Actin are not uniformly distributed across monolayers</u>
396 As our model suggested that non-uniformity of contractility could reconcile our
397 experimental observations, we decided to examine contractility within the monolayers. We
398 measured phosphorylated myosin light chain II (pMyoII) intensity across the monolayers as
399 a proxy for contractility[20], but also examined actin architecture which plays an essential role

400 in cell mechanics[7]. As traction and intercellular stresses are dependent on myosin
401 activity[20,57], we initially wanted to examine if the total intensity of pMyoII altered depending
402 on the pattern and substrate stiffness. To minimise experimental variation, we processed all
403 independent samples in parallel to allow direct comparison in intensity using widefield
404 imaging for speed. Measuring the intensity of DAPI (Fig. 5b,c), we observed consistent
405 results with our cell count data (Fig. 1i,j). Examining F-Actin revealed that on disks there is a
406 consistent level of F-Actin, that appears to be linked to cell number (Fig. 5d). However, on
407 rings we observe a slight decrease in total F-Actin intensity as substrate stiffness increases
408 (Fig. 5e). Next, we examined total intensity of pMyoII which for both patterns revealed a
409 decrease as substrate stiffness increases, but more pronounced for rings (Fig. 5f,g). This
410 agrees with our fitted model parameters which predicted a reduction in overall contractility
411 as substrate stiffness increased (Fig. 4c,h).
412 To examine the spatial distribution of pMyoII, we imaged samples with improved
413 optical resolution. Examining the total pMyoII intensity of z-sections across our monolayers
414 we did observe spatial variation in pMyoII to varying degrees on our monolayers (Fig. 5h-k).
415 For disk patterns, pMyoII intensity appeared more localised at the monolayer edge on soft
416 hydrogels, becoming more uniform on stiffer hydrogels (Fig. 5h,i). For rings, the opposite
417 trend in pMyoII intensity distribution was observed, with a more uniform distribution on
418 soft hydrogels becoming more localised to the edge on stiffer hydrogels (Fig. 5j,k). As
419 intensity was variable between samples, we normalised pixel intensity to the mean intensity
420 within the ablation ROI (40-50μm) to quantify the spatial distribution of pMyoII (Fig. 5l-q).
421 This revealed that no condition had a uniform localisation, with radial variation always
422 present (Fig. 5l-q), however, there was a redistribution of pMyoII for both patterns as
423 substrate stiffness increases. On disks there was a reduction in pMyoII intensity outside the
424 ablation ROI (Fig. 5p), whilst on rings an increase was observed (Fig. 5q). Measuring the
425 percentage difference in pMyoII intensity between the edge and central regions (Fig. 5r)
426 revealed a behaviour similar to that predicted by our model (Fig. 5a); as substrate stiffness
427 increased, on disk patterns there is a trend for pMyoII to become more uniform but on rings
428 patterns there is a trend to become more localised at the edge.
429 As there are minor differences in cell height on ring patterns (Fig. 1l), we wanted to
430 determine if cell height was an issue in this analysis. We therefore examined pMyoII
431 localisation across the cell height which revealed that it was predominantly localised basally

432 (Fig. S4a-c). Consequently, we examined actomyosin distribution across the monolayers
433 focusing only on the basal layer (Fig. S4d-l). Examining pMyoII we observed similar changes
434 in distribution across the basal layer as we did the whole monolayer (Fig. S4j-l), suggesting
435 that cell height wasn't confounding our analysis. Interestingly, this analysis revealed drastic
436 changes in the distribution of the actin cytoskeleton between patterns (Fig. S4d-i) which was
437 masked when examining total intensity, as F-actin tended to be more localised along cell
438 junctions (Fig. S4a-c). On disk patterns, cells at the periphery extended lamella outwardly
439 leading to a dense band of F-Actin at the edge (Fig. S4d,f,h). This was followed by a
440 reduction in F-Actin behind this band, as cell nuclei aligned close to the edge, with the more
441 centrally located cells exhibiting clear fibres that spanned the cell width and were
442 predominantly located near active focal adhesions (Fig. S4m, m'). On ring patterns, an F-
443 Actin bundle spanning the monolayer perimeter was observed, with a reduction in F-Actin
444 along the laminin ring, and another accumulation at the inner ring diameter but not as a
445 defined actin bundle (Fig. S4e,g,i). The architecture of the actin cytoskeleton is critical for
446 generating[58] and transmitting[17] stresses, and the differences between ring and disk patterns
447 highlights how altering focal adhesion distribution drastically alters the mechanical
448 equilibrium of the tissue.
449 Overall, reconciling the model and experimental observations, we find that the
450 relationship between traction and intercellular stress is not universal but changes in
451 response to both the distribution of focal adhesions and compliance of the substrate. This is
452 due to cellular contractility adapting, to generate a tissue-wide force balance.

453 **Discussion**

454 The control of a tissue's mechanical equilibrium is essential for the regulation of a
455 wide array of physiological processes such as morphogenesis[1] or wound healing[3], and when
456 disturbed can lead to disease progression[59]. Here we investigated the relationship between
457 applied surface traction and intercellular stresses specifically focusing on the role of focal
458 adhesions in the mechanical equilibrium of epithelial monolayers. We find that, for ring
459 patterns where focal adhesion distribution is non-uniform, epithelial monolayer stresses do
460 not conform to the intuition that the relationship between traction and intercellular stresses
461 is linear (Fig. 3m,n). Instead, while traction forces do not change upon increased substrate
462 stiffness (Fig. 2f,h), intercellular tension as measured by laser ablation dramatically drops
463 (Fig. 3l). To reconcile experimental observations with the monolayers being at force-
464 balance, we proposed and confirmed that spatial patterns in contractility emerge (Fig. 4, 5).

465 What is the origin of this apparently counter-intuitive behaviour? In comparison with
466 single cell studies, for large clusters of cells, forces can be distributed differently between
467 the cells and substrate according to the state of cell-cell junctions[55,60] and the distribution of
468 cell-ECM attachments[16]. In particular, attachment to the ECM has been shown to effectively
469 decrease the length-scale of stress transmission[30], so differences in substrate stiffness can
470 potentially be transmitted to cell-cell junctions over longer distances if cells are not all
471 anchored to the matrix. Conversely, as with the disk patterns where focal adhesions are
472 widely distributed (Fig. 1g), often near cell-cell junctions (Fig 1e) and associated to the
473 contractile acto-myosin network (Fig. S4m), cell-generated forces are most likely
474 transmitted locally to the substrate. In this situation the mechanical properties of the
475 substrate become important for stress transmission across the tissue, as has previously
476 been reported for fibroblasts[61]. Indeed, we found that on disk patterns the monolayer was
477 less able to deform stiffer hydrogels (Fig. 2c), and this was accompanied by a decrease in
478 total traction (Fig. 2e). This is associated with a reduction in the overall total contractility of
479 the layer on stiffer gels (lower pMyoII total intensity, Fig. 5f) as predicted by our theoretical
480 model (Fig. 4c). On soft conditions however, mechanical stress propagates further across
481 the monolayer as cells are more able to deform the substrate locally (Fig. S2e), and higher
482 total contractility is observed (Fig. 5f). This is accompanied with contractile activity
483 differentially localised most strongly to the edge of the layer (fig. 5l,p) where the highest
484 deformations were measured (Fig. S2e).

485

486 In contrast, for ring patterns on increasing substrate stiffness, traction stress is
487 relatively stable (Fig. 2f,h) whilst intercellular tension decreases (Fig. 3l), highlighting that
488 different mechanical states are reached. For rings, it is only the cells at the edge of the
489 monolayer that can form focal adhesions and directly experience gel deformability (Fig. 1h).
490 The bulk of the monolayer can now only contribute predominantly to stress distribution
491 through cell-cell junctions. Similar to the disk patterns, there is still a decrease in
492 deformation on stiffer gels (Fig. 2d) and a corresponding decrease in total contractile
493 activity of the monolayer (lower pMyoII total intensity, Fig. 5g). However, the non-uniform
494 adhesion distribution generates a marked shift in the collective behaviour of the tissue.
495 With increasing stiffness, the mechanical activity becomes progressively more localised to
496 the edge of the monolayer on stiffer gels (Fig. 5r), thus generating lower internal stress as
497 observed and predicted (Fig. 4k). The stronger resistance to deformation of stiffer gels has
498 an anchoring effect on the outer ring, but now the balance of resistive forces with the
499 unadhered cells adjacent to these ring cells is altered. These results emphasise that the
500 processes contributing to force transmission throughout a monolayer cannot be isolated to
501 a single cell without considering their collective effects. This is highlighted by changes in F-
502 Actin architecture across the monolayer between disk and ring patterns (Fig. S4).
503 Changes in the spatial distribution of actomyosin contractility underpins the
504 response to differential adhesion on our ring and disk patterns (Fig. 4, 5). Spatial distribution
505 of contractility has been observed in single cells[62,63] linked to focal adhesion signalling[62],
506 however for epithelial monolayers, whilst radial patterns of focal adhesion distribution have
507 been reported[64], to our knowledge this has not been linked to non-uniform patterns of
508 contractility. Spatial variation in myosin have been observed *in vivo*, but these are normally
509 examined in the context of morphogenesis[65] or generating cell-population boundaries[66] and
510 not linked to cell-ECM attachments. We recently observed in the *Drosophila* abdominal
511 epidermis that a tissue-wide spatial pattern of myosin arises during the pupal stages as the
512 ECM is degraded[27] but whether this is important for the tissue's mechanical equilibrium is
513 not known. However, the emergence of spatial patterns of contractility in our monolayers
514 has important implications on the application of force inference techniques. To examine
515 intercellular stresses of a monolayer, inference methods such as monolayer force
516 microscopy (MSM)[10,11,18] or Bayesian inversion stress microscopy (BISM[12]) have been

517 developed. These techniques infer intercellular stresses based on traction forces measured
518 and can estimate spatial variation in intercellular stresses in a non-destructive manner,
519 unlike laser ablation, allowing long-term analysis to be made. The implementation of these
520 techniques often assumes a passive elastic model linking traction and intercellular
521 stresses[10,11,13,17,67]. For MDCK cell-doublets, where focal adhesions have been shown to
522 disassemble along cell-cell contacts[68], the direct balance of traction forces with cell-cell
523 adhesions potentially holds[14]. However, even in these simple cell-doublet systems the
524 distribution of focal adhesions can drastically alter the propagation of forces. For instance,
525 cardiomyocyte doublets seeded or cultured on 90kPa substrates generated focal adhesions
526 at the site of cell-cell junctions, impairing mechanical coupling and force propagation[15]. This
527 highlights the importance of examining the distribution of focal adhesions when inferring
528 stress transmission. Moreover, on our 200μm diameter disk micropatterns, we observed
529 spatial variation in pFAK with some regions having higher intensity than others (see Fig 1c).
530 Considering a larger tissue, the distribution of focal adhesions could vary drastically even on
531 a uniform substrate, altering the local mechanical equilibrium in that region of a tissue. This
532 would impact whether local intercellular stresses were positively correlated with traction
533 stress or not. Indeed, analysis of epithelial monolayers showed a “rugged landscape” of
534 traction forces[10], and spatial patterns of ECM composition and properties have been
535 observed in developmental and pathological situations[41]. Therefore, when employing
536 techniques such as MSM and BISM it is important to not only examine the variation in local
537 distribution of focal adhesions, but also spatial variation in contractility to confidently infer
538 intercellular stresses as a function of the mechanical activity of the tissue as a whole.

539 **Methods**
540
541 **Cell culture**
542 EpH4 cells with Cas9 inserted into the Rosa26 locus (kind gift from high throughput
543 screening STP, Francis Crick Institute) were cultured in 4.5g l^{-1} Dulbecco's modified Eagle
544 medium (Gibco, Thermo Fisher Scientific) containing 10% foetal bovine serum (Sigma-
545 Aldrich, Merck) and 1% penicillin-streptavidin (Gibco, Thermo Fisher Scientific). For seeding
546 on hydrogels, 180,000 cells in 2ml of culture medium were centrifuged at 80 r.c.f for 5
547 minutes. Cells were cultured for 2 hours and then extensively washed in PBS to remove non-
548 adherent cells and 2ml of fresh media was added. Cells were incubated for 48 hours, to
549 proliferate and cover the micropatterns. For live-imaging experiments, cells were washed in
550 PBS and then labelled for 15 minutes with 1.5μl CellMask Green (Thermo Fisher Scientific),
551 diluted and vortexed in 1.5ml FluoroBrite DMEM (Gibco, Thermo Fisher Scientific)
552 containing 1% penicillin-streptavidin but no FBS. Media was then replaced with 1.5ml
553 FluoroBrite DMEM media as described, ready for imaging.
554
555 **Micropatterning of methacrylated hyaluronic acid hydrogels**
556 3g of methacrylated hyaluronic acid (MeHA) was synthesised as previously described[43], with
557 a methacrylate modification of hyaluronic acid monomer between 76 – 79% as
558 characterised through ^{1}H NMR (Fig. S1a). MeHA hydrogels were formed at a concentration
559 of 3 wt% and crosslinked with increasing amounts of dithiothreitol (DTT) to modulate
560 substrate rigidity. Specifically, hydrogels were formed within a 250μm high silicon gasket
561 with a 16mm inner diameter and outer diameter of 18mm, sandwiched between a 19mm
562 micropatterned coverslip and a silanized glass surface. Hydrogels were incubated with 5%
563 BSA (Tocris Bioscience) in PBS for 2 hours before seeding cells.
564
565 Micropatterned coverslips were generated by plasma-activating 18mm coverslips and
566 coating in 0.1mg ml^{-1} poly-L-lysine poly(ethylene glycol) (PLL(20) – g[3.5]-PEG(2), SuSoS)
567 suspended in 10mM HEPES buffer at pH7.4. To pattern the coverslips, a quartz photomask
568 (Compugraphics) and UVO-cleaner (Jelight) were used to remove PLL-g-PEG from the
569 surface of the coverslip. Patterned coverslips were then incubated for 30 minutes with
570 laminin diluted in 100mM sodium bicarbonate buffer at pH7.4. Laminin consisted of either

571 20μg ml^{-1} laminin (Sigma-Aldrich, Merck) solution or 20μg ml^{-1} 2:1 mix of laminin and
572 laminin-labelled with alexa633 for live-imaging and immunostaining, respectively. To label
573 laminin, 500μl of 1mg ml^{-1} laminin solution was injected into a Slide-A-Lyzer (Thermo Fisher
574 Scientific) and dialysed two times in 1L of PBS at 4° C and stirred at a low shear rate for 24
575 hours. The dialysed laminin was then labelled with Alexa633 following the manufacturers
576 protocol (Thermo Fisher Scientific). Micropatterns were either repeating patterns of disks
577 with a diameter of 200μm, or rings with an outer diameter of 200μm and inner diameter of
578 160μm.
579
580 For silanized glass surfaces, either No. 1.5 glass bottom 35mm μ-dishes high (Ibidi) or 20mm
581 diameter uncoated 6-well plates (Mattek) were employed for live-imaging or
582 immunostainings, respectively. Glass surfaces were plasma-activated and silanized with (3-
583 aminopropyl) trimethoxysilane (VWR) and 5% glutaraldehyde (VWR).
584
585 **Atomic force microscopy**
586 Gels were generated as described but using non-patterned, passivated coverslips and No.
587 1.5 50mm dish with 30mm uncoated glass diameter (Mattek). Force curves were measured
588 on a JPK Nanowizard 4 using a CP-qp-CONT-Au-B-5 cantilever probe (sQube, NanoAndMore
589 GMBH). Measurements were taken in four regions per hydrogel (two at the periphery and
590 two central) with 50 indentations over a 100μm x 100μm grid. The number of hydrogels
591 quantified for each DTT concentration was 7 for 6.30 to 15.75mM and 6 for 18.9mM. Force
592 curves were made with an extend speed of 2μm s^{-1} and a setpoint (8 – 25nN, depending on
593 substrate stiffness) set to achieve a maximum indentation depth of ~500nm. The young's
594 modulus was calculated by fitting a Hertz model using the AFM_Youngs_modulus_fit
595 programme developed by Dr Stefania Marcotti (available on GitHub:
596 https://github.com/INSIGNEO/AFM_Youngs_modulus_fit), at different indentation depths
597 (Fig. S1b). A standard indentation depth of 250nm across all hydrogel conditions was used
598 to calculate the Young's modulus, as it is within the linear phase of the modulus versus
599 indentation depth for all hydrogel conditions and is 1/1000 of the hydrogel thickness.
600
601 **Traction force microscopy**

602 Crimson labelled 0.2μm carboxylate modified FluoSpheres (Thermo Fisher Scientific) were
603 mixed with MeHA hydrogel precursor solution with a 1:40 ratio prior to crosslinking with
604 DTT. Images were acquired as detailed below. After live-imaging, cells were treated with 10x
605 trypsin-EDTA, no-phenol red (Gibco) until cells detach from the hydrogels and a final
606 reference frame acquired.
607
608 **Laser ablation**
609 Images were acquired on a Zeiss LSM 780 system with an LD C-Apochromat 40x NA 1.1
610 water objective and 0.8 zoom, so that micropatterns could be acquired in a single 512 x 512
611 pixel tile. Z-stacks were acquired by measuring excitation by 480nm and 633nm lasers
612 simultaneously for z-slices every 1μm, spaced between 5 - 6μm below the hydrogel surface
613 and 10 - 12μm above. Z-stacks were acquired every 10 seconds for one minute before a
614 laser ablation and five minutes afterwards. An annulus ROI was generated using the
615 freehand tool and had an internal diameter of 80μm (154 pixels) – approximately 4 – 6 cells
616 in diameter – and external diameter of 100μm (193 pixels) – leaving 3 – 4 cells at the
617 periphery. Ablations were made in a z-plane positioned in the middle of the epithelial layer
618 (3 - 6μm from the hydrogel surface) with a Coherent Chameleon NIR tuneable laser set at
619 780nm and 40% - 60% power output and lasted ~6.7ms.
620
621 **Immunostaining**
622 Samples were fixed in 4%-paraformaldehyde (TAAB) for 15 minutes and permeabilised with
623 0.3% Triton X-100 for 5 minutes, covered from light. Samples were then blocked with 10%
624 neonatal goat serum (Generon) for an hour at room temperature and incubated with
625 primary antibodies diluted in 10% neonatal goat serum at 4° C overnight. Samples were
626 then incubated in secondary antibodies, Phalloidin-Alexa568 (Thermo Fisher Scientific,
627 #A12380: dilution 1:400) and DAPI (1000x stock solution; Sigma) for 1 hour at room
628 temperature. Samples were washed and stored in 0.1% Triton X-100. For batch processing
629 of all samples to examine total pMyoII levels, images were acquired on a Zeiss
630 Celldiscoverer 7 widefield system with a Zeiss Plan-Apochromat 20x NA 0.7 Autocorr
631 objective with 1x zoom and 2240 x 2254 pixels and a x-y resolution 0.1747602 for a single
632 plane. To examine spatial localisation of proteins of interest, samples were imaged on a

633 Nikon CSU-W1 spinning disk with an Apo LWD 40x WI λS DIC N2 NA 1.15 objective with
634 1200 x 1200 pixels and a x-y resolution of 0.2731993μm. Z-slices were acquired 0.4μm apart
635 for each channel sequentially. The following antibodies were used, mouse anti-phospho-
636 Myosin Light Chain 2 (Ser19) (Cell Signalling Technology, #3675: dilution 1:200), rabbit anti-
637 phospho-FAK (Tyr397) (Thermo Fisher Scientific, 44-624G: dilution 1:400), mouse anti-E-
638 Cadherin (BD Transduction #610182: dilution 1:400), Goat anti-mouse IgG H&L Alexa 405
639 (Abcam, #175660: dilution 1:400), and Goat anti-rabbit IgG H&L Alexa 488 (Thermo Fisher
640 Scientific, #A-11008: dilution 1:400). F-Actin was stained with Alexa Fluor 568 Phalloidin
641 (Thermo Fisher Scientific, #A-12380) along with the secondary antibodies.
642
643 **Data analysis**
644 All images were processed and analysed in Fiji, Mathworks MATLAB and Wolfram
645 Mathematica.
646
647 Traction force microscopy pipeline
648 Images were acquired as detailed above. After adding trypsin to detach cells, there is slight
649 stage movement in the in x, y and z directions. Therefore, all movies were registered with
650 the trypsin frame as a reference. For z registration, the surface of the hydrogel was
651 calculated by examining the total intensity across the image in 24x24 pixel blocks for each z-
652 slice, with the surface for each block set by the last slice with a signal. To project on a pixel-
653 by-pixel basis, a Gaussian Filter was employed across all blocks and then rounded, to
654 minimise any jumps in z-plane. A maximum projection of the beads was then calculated for
655 both the movie and trypsin reference frame from the surface to the same number of z-slices
656 below the surface set by the least number of frames available, normally 3 - 4 slices. Once z-
657 registration is complete the trypsin frame was added as the final frame of the movie and
658 registered in Fiji with the StackReg macro, using the last frame as the reference. Bead
659 displacement, traction forces and strain energy were calculated using the TFM package
660 developed by Gaudenz Danuser's group[53], using a 31x31 pixel template size and L-
661 parameterisation of 0.00000001.
662
663 Laser ablation analysis

664 Initially a projection of the cell mask was generated by identifying the ablation plane and
665 calculating a maximum projection between two slices above and below this frame. The
666 ablation plane was identified by measuring the loss of intensity within the ablation ROI for
667 each frame after the ablation and selecting the frame with the biggest loss. To measure the
668 recoil velocity, the Mathematica ImageFeatureTrack function was employed with specifying
669 features in every pixel and filtering pixels where no motion was detected. To measure
670 maximum recoil velocity for each movie, the recoil velocity value for the 95th percentile
671 across the entire field of view was taken (see Fig. S3).
672
673 Cell morphology quantification
674 To measure cell elongation and area, projections generated for analysing the recoil velocity
675 were segmented through Skeletor[27] and manually corrected in Fiji. Using a watershed
676 algorithm in Mathematica, cell area and elongation (1-width/length) were measured. To
677 measure cell height, all immunostaining experiments were combined, and an orthogonal
678 projection made using the Fiji macro with a box ROI 20 x 850 pixels centred on the
679 monolayer centroid in both the x and y direction. In Mathematica, cell height was measured
680 by combining F-Actin intensity with either pMyoII or E-Cad intensity for the orthogonal
681 projections, depending on the experiments, and binarizing based on pixels whose intensity
682 was greater than the mean plus four standard deviations of the entire projected image. A
683 FillingTransform and DeleteSmallComponents function were applied to clean up the
684 binarization so only the monolayer remained.
685
686 Membrane intensity changes
687 To measure the movement of the epithelium in our movies before the ablation to
688 determine their dynamics, the frame immediately before the ablation was subtracted from
689 the initial frame and the remaining pixel values summed and normalised to the original
690 summed pixel values. A value close to zero highlights very little movement within the
691 epithelium.
692
693 Basal projection algorithm
694 To quantify just the basal layer of the monolayers we used Laminin labelling to identify the
695 surface of the hydrogel. We selected a z-slice for each pixel that corresponded to the

696 highest laminin intensity, after noise-filtering the z-intensity profile with a LowpassFilter. We
697 then generated a contour map by smoothening the pixel values with a GaussianFilter,
698 before rounding to a whole number to correspond to a z-slice. Based on this contour map,
699 we then did a maximum projection over three z-slices, one above and one below our
700 contour map value.
701
702 pFAK segmentation
703 To quantify adhesion coverage and size, pFAK images were binarized based on pixel
704 intensity value in Mathematica. Due to variable background intensity across the field of
705 view, a MedianFilter was applied with a 61 pixel-by-pixel sliding window and subtracted
706 from the original image. A background threshold value was then calculated by measuring
707 the mean intensity plus two standard deviations of pixels outside the micropatterned region
708 which was determined based on the laminin micropattern channel. Any pixel which had a
709 higher intensity value than the background threshold was binarized. To de-noise the binary
710 image, isolated binarized pixels were removed using the DeleteSmallComponents function
711 with a value set to 1.
712
713 Statistical analysis
714 All statistics were performed in Mathematica using the LocationEquivalenceTest function
715 which tests the null hypothesis that populations are equal choosing the most powerful test
716 that applies to the data. The most common test applied was the Kruskal Wallis test as often
717 one condition would fail normality tests. If the LocationEquivalenceTest was significant a
718 post-test Mann-Whitney was performed comparing the value on the softest substrate to all
719 other substrate stiffnesses. For trend fitting, the LinearModelFit function was used on the
720 mean values for each population with a confidence interval of 95%. The model with the
721 greatest R^2-value was selected.
722
723 For all statistical values used in the analysis, see Tables S1&2 in Supplementary Information.
724
725 **Theoretical modelling**
726 We describe the theoretical and computational modelling briefly here, for a more detailed
727 description see the additional supplementary information.

728

729 Active matter model for the cell layer

730 An active matter model was used to predict the deformations and stresses in the cell layer.
731 This widely adopted approach incorporates an active cell-generated stress additively into
732 the constitutive relation of the cell material, see[36,37,39,54]. As such we assumed a constitutive
733 relation such that the stress $\boldsymbol{s} = \boldsymbol{s}_{\text{passive elastic}} + \boldsymbol{s}_{\text{active}}$, as Fig. 3a specifically in tensor notation
734 this gives:

$$\sigma_{ij} = \frac{hE}{1+\nu}\left(\epsilon_{ij} + \frac{\nu}{1-\nu}\epsilon_{kk}\delta_{ij}\right) + \frac{hE}{2(1-\nu)}P(\mathbf{x})\delta_{ij},$$

735

736 where we use the summation convention and introduce the kronecker delta. The active contractility
737 P(x) is assumed to act isotropically. The deformations are then determined from the force balance

$$\nabla \cdot \sigma - KT(\mathbf{x})\mathbf{u} = \mathbf{0},$$

738

739 Where K quantifies substrate resistance to deformation and $T(\mathrm{x})$ is an indicator function
740 that take the value of 1 where the cell is adhered and 0 otherwise. The contractility function
741 is assumed to be constant throughout the layer $P(\mathrm{x})=P_{\mathrm{a}}$, for Fig. 3, with the addition of a
742 monotonic increasing contractility profile $P(\mathrm{x})=a(1+b\mathrm{r}^5)$ for Fig. 4. The polynomial
743 contractility profile is selected to enable analytical phase plane analysis. Where adhesion is
744 uniform analytical solutions of the force balance equation may be obtained by standard
745 techniques as the resulting equations are of Bessel type and solutions may be obtained by
746 variation of parameters. Where non-uniform adhesion is observed numerical solutions of
747 the force balance equation are obtained using finite element methods within the MATLAB
748 PDE Toolbox.

749

750 Adhesion geometry

751 For uniform adhesion the indicator function is either taken as unity throughout for the disk
752 geometry or as unity in the ring region. Where adhesion is informed by the pFAK data (Fig.
753 1) and modelled as non-uniform we take the resulting adhesion geometry is as in Fig. 1h.
754 Specifically, we consider two thin annuli of thickness r_t=0.06 at the edges of the
755 micropatterned ring corresponding to the regions with highest intensity pFAK. Additionally,
756 we set a distribution of adhered spots in the internal region and between the two annuli as
757 the pFAK intensity is non-zero in these regions; spots between the two annuli have a radius

of r_s=0.0167r_0 and in the internal region have radius r_s=0.018r_0. In these adhered regions T(x)=1 and elsewhere we set T(x)=0.

Acknowledgements

We would like to thank the Ok-Ryul Song and Michael Howell from the High-throughput screening STP at the Francis Crick Institute for sharing the EpH4-Cas9 cells. We are grateful to Matt Renshaw from the Crick CALM STP, and Ravi Desai and Christina Dix from the Crick Making STP for their assistance. We thank the bioAFM and bioImaging facilities within FBMH at the University of Manchester. We are grateful to Stefania Marcotti, Richard Thorogood, Nigel Hodson, Olivia Courbot and Alberto Elosegui-Artola for advice on the analysis of AFM data. We thank Guillaume Charras and Alberto Elosegui-Artola for comments on the manuscript. JRD was supported by a Wellcome Trust Sir Henry Wellcome fellowship (201358/Z/16/Z) and University of Manchester Dean's Prize. JSW was supported by postdoctoral EPSRC funding (EP/W522302/1). This work was supported by a Wellcome Trust Investigator award (107885/Z/15/Z) to NT. Work in the Tapon lab is supported by the Francis Crick Institute, which receives its core funding from Cancer Research UK (CC2138), the UK Medical Research Council (CC2138), and the Wellcome Trust (CC2138). For Open Access, the authors have applied a CC BY public copyright licence to any Author Accepted Manuscript version arising from this submission.

1. Clarke, D. N. & Martin, A. C. Actin-based force generation and cell adhesion in tissue morphogenesis. *Current Biology* **31**, R667–R680 (2021).
2. Pandya, P., Orgaz, J. L. & Sanz-Moreno, V. Actomyosin contractility and collective migration: may the force be with you. *Curr Opin Cell Biol* **48**, 87–96 (2017).
3. Lim, S. E., Vicente-Munuera, P. & Mao, Y. Forced back into shape: Mechanics of epithelial wound repair. *Curr Opin Cell Biol* **87**, 102324 (2024).
4. Mao, Y. & Baum, B. Tug of war-The influence of opposing physical forces on epithelial cell morphology. *Dev Biol* **401**, 92–102 (2015).
5. Romani, P., Valcarcel-Jimenez, L., Frezza, C. & Dupont, S. Crosstalk between mechanotransduction and metabolism. *Nat Rev Mol Cell Biol* (2020) doi:10.1038/s41580-020-00306-w.
6. Dupont, S. & Wickström, S. A. Mechanical regulation of chromatin and transcription. *Nature Reviews Genetics* vol. 23 624–643 Preprint at https://doi.org/10.1038/s41576-022-00493-6 (2022).
7. Sun, X. & Alushin, G. M. Cellular force-sensing through actin filaments. *FEBS Journal* **290**, 2576–2589 (2023).
8. Gómez-González, M., Latorre, E., Arroyo, M. & Trepat, X. Measuring mechanical stress in living tissues. *Nature Reviews Physics* **2**, 300–317 (2020).
9. Lekka, M., Gnanachandran, K., Kubiak, A., Zieliński, T. & Zemła, J. Traction force microscopy – Measuring the forces exerted by cells. *Micron* **150**, (2021).
10. Tambe, D. T. *et al.* Collective cell guidance by cooperative intercellular forces. *Nat Mater* **10**, 469–75 (2011).
11. Tambe, D. T. *et al.* Monolayer Stress Microscopy: Limitations, Artifacts, and Accuracy of Recovered Intercellular Stresses. *PLoS One* **8**, e55172 (2013).
12. Nier, V. *et al.* Inference of Internal Stress in a Cell Monolayer. *Biophys J* **110**, 1625–1635 (2016).
13. Ng, M. R., Besser, A., Brugge, J. S. & Danuser, G. Mapping the dynamics of force transduction at cell-cell junctions of epithelial clusters. *Elife* **3**, e03282 (2014).
14. Maruthamuthu, V., Sabass, B., Schwarz, U. S. & Gardel, M. L. Cell-ECM traction force modulates endogenous tension at cell-cell contacts. *Proceedings of the National Academy of Sciences* **108**, 4708–4713 (2011).
15. McCain, M. L., Lee, H., Aratyn-Schaus, Y., Kléber, A. G. & Parker, K. K. Cooperative coupling of cell-matrix and cell-cell adhesions in cardiac muscle. *Proc Natl Acad Sci U S A* **109**, 9881–9886 (2012).
16. Sim, J. Y. *et al.* Spatial distribution of cell-cell and cell-ECM adhesions regulates force balance while main taining E-cadherin molecular tension in cell pairs. *Mol Biol Cell* **26**, 2456–2465 (2015).
17. Ruppel, A. *et al.* Force propagation between epithelial cells depends on active coupling and mechano-structural polarization. *Elife* **12**, 1–42 (2023).
18. Trepat, X. *et al.* Physical forces during collective cell migration. *Nat Phys* **5**, 426–430 (2009).
19. Balasubramaniam, L. *et al.* Investigating the nature of active forces in tissues reveals how contractile cells can form extensile monolayers. *Nat Mater* **20**, 1156–1166 (2021).
20. Vincent, R. *et al.* Active Tensile Modulus of an Epithelial Monolayer. *Phys Rev Lett* **115**, (2015).

21. Serra-Picamal, X. *et al.* Mechanical waves during tissue expansion. *Nat Phys* **8**, 628–634 (2012).
22. Haas, A. J. *et al.* Interplay between Extracellular Matrix Stiffness and JAM-A Regulates Mechanical Load on ZO-1 and Tight Junction Assembly. *Cell Rep* **32**, 107924 (2020).
23. Mohan, A. *et al.* Spatial Proliferation of Epithelial Cells Is Regulated by E-Cadherin Force. *Biophys J* **115**, 853–864 (2018).
24. Gayrard, C., Bernaudin, C., Déjardin, T., Seiler, C. & Borghi, N. Src- and confinement-dependent FAK activation causes E-cadherin relaxation and β-catenin activity. *Journal of Cell Biology* **217**, 1063–1077 (2018).
25. Bonnet, I. *et al.* Mechanical state, material properties and continuous description of an epithelial tissue. *J R Soc Interface* **9**, 2614–2623 (2012).
26. Bambardekar, K., Clément, R., Blanc, O., Chardès, C. & Lenne, P.-F. Direct laser manipulation reveals the mechanics of cell contacts in vivo. *Proceedings of the National Academy of Sciences* **112**, 1416–1421 (2015).
27. Davis, J. R. *et al.* ECM degradation in the Drosophila abdominal epidermis initiates tissue growth that ceases with rapid cell-cycle exit. *Current Biology* **32**, 1285-1300.e4 (2022).
28. Sonam, S. *et al.* Mechanical stress driven by rigidity sensing governs epithelial stability. *Nat Phys* **19**, 132–141 (2023).
29. Vazquez, K., Saraswathibhatla, A. & Notbohm, J. Effect of substrate stiffness on friction in collective cell migration. *Sci Rep* **12**, (2022).
30. Goodwin, K. *et al.* Basal Cell-Extracellular Matrix Adhesion Regulates Force Transmission during Tissue Morphogenesis. *Dev Cell* **39**, 611–625 (2016).
31. Green, Y., Fredberg, J. J. & Butler, J. P. Relationship between velocities, tractions, and intercellular stresses in the migrating epithelial monolayer. *Phys Rev E* **101**, (2020).
32. Friedrich, B. M. & Safran, S. A. How cells feel their substrate: Spontaneous symmetry breaking of active surface stresses. *Soft Matter* **8**, 3223–3230 (2012).
33. Yang, W., Luo, M., Gao, Y., Feng, X. & Chen, J. Mechanosensing model of fibroblast cells adhered on a substrate with varying stiffness and thickness. *J Mech Phys Solids* **171**, (2023).
34. Mertz, A. F. *et al.* Scaling of Traction Forces with the Size of Cohesive Cell Colonies. *Phys Rev Lett* **108**, 198101 (2012).
35. Banerjee, S. & Marchetti, M. C. Contractile Stresses in Cohesive Cell Layers on Finite-Thickness Substrates. *Phys Rev Lett* **109**, 108101 (2012).
36. Edwards, C. M. & Schwarz, U. S. Force localization in contracting cell layers. *Phys Rev Lett* **107**, 1–5 (2011).
37. Prost, J., Jülicher, F. & Joanny, J. F. Active gel physics. *Nat Phys* **11**, 111–117 (2015).
38. Oakes, P. W., Banerjee, S., Marchetti, M. C. & Gardel, M. L. Geometry regulates traction stresses in adherent cells. *Biophys J* **107**, 825–833 (2014).
39. Solowiej-Wedderburn, J. & Dunlop, C. M. Sticking around: Cell adhesion patterning for energy minimization and substrate mechanosensing. *Biophys J* **121**, 1777–1786 (2022).
40. Reinhart-King, C. A., Dembo, M. & Hammer, D. A. Cell-cell mechanical communication through compliant substrates. *Biophys J* **95**, 6044–6051 (2008).
41. Kozyrina, A. N., Piskova, T. & Di Russo, J. Mechanobiology of Epithelia From the Perspective of Extracellular Matrix Heterogeneity. *Front Bioeng Biotechnol* **8**, (2020).

42. Reichmann, E., Ball, R., Groner, B. & Friis, R. R. New mammary epithelial and fibroblastic cell clones in coculture form structures competent to differentiate functionally. *J Cell Biol* **108**, 1127–1138 (1989).
43. Guvendiren, M. & Burdick, J. A. Stiffening hydrogels to probe short- and long-term cellular responses to dynamic mechanics. *Nat Commun* **3**, 792 (2012).
44. Lopez, J. I., Kang, I., You, W. K., McDonald, D. M. & Weaver, V. M. In situ force mapping of mammary gland transformation. *Integrative Biology* **3**, 910–921 (2011).
45. Maschler, S. M. *et al.* Tumor cell invasiveness correlates with changes in integrin expression and localization. *Oncogene* **24**, 2032–2041 (2005).
46. Loebel, C., Mauck, R. L. & Burdick, J. A. Local nascent protein deposition and remodelling guide mesenchymal stromal cell mechanosensing and fate in three-dimensional hydrogels. *Nat Mater* **18**, 883–891 (2019).
47. Loebel, C. *et al.* Metabolic labeling of secreted matrix to investigate cell–material interactions in tissue engineering and mechanobiology. *Nature Protocols* vol. 17 618–648 Preprint at https://doi.org/10.1038/s41596-021-00652-9 (2022).
48. Kwon, M. Y. *et al.* Influence of hyaluronic acid modification on CD44 binding towards the design of hydrogel biomaterials. *Biomaterials* **222**, 119451 (2019).
49. Kechagia, J. Z., Ivaska, J. & Roca-Cusachs, P. Integrins as biomechanical sensors of the microenvironment. *Nat Rev Mol Cell Biol* **20**, 457–473 (2019).
50. Han, S. J., Bielawski, K. S., Ting, L. H., Rodriguez, M. L. & Sniadecki, N. J. Decoupling substrate stiffness, spread area, and micropost density: A close spatial relationship between traction forces and focal adhesions. *Biophys J* **103**, 640–648 (2012).
51. Fusco, S., Panzetta, V. & Netti, P. A. Mechanosensing of substrate stiffness regulates focal adhesions dynamics in cell. *Meccanica* **52**, 3389–3398 (2017).
52. Panzetta, V., Fusco, S. & Netti, P. A. Cell mechanosensing is regulated by substrate strain energy rather than stiffness. *Proc Natl Acad Sci U S A* **116**, 22004–22013 (2019).
53. Han, S. J., Oak, Y., Groisman, A. & Danuser, G. Traction microscopy to identify force modulation in subresolution adhesions. *Nat Methods* **12**, 653–656 (2015).
54. Solowiej-Wedderburn, J. & Dunlop, C. M. Cell-strain-energy costs of active control of contractility. *Phys Rev E* **107**, (2023).
55. Mertz, A. F. *et al.* Cadherin-based intercellular adhesions organize epithelial cell-matrix traction forces. *Proc Natl Acad Sci U S A* **110**, 842–847 (2013).
56. Rheinlaender, J. *et al.* Cortical cell stiffness is independent of substrate mechanics. *Nat Mater* **19**, 1019–1025 (2020).
57. Valon, L., Marín-Llauradó, A., Wyatt, T., Charras, G. & Trepat, X. Optogenetic control of cellular forces and mechanotransduction. *Nat Commun* **8**, (2017).
58. Doss, B. L. *et al.* Cell response to substrate rigidity is regulated by active and passive cytoskeletal stress. *Proc Natl Acad Sci U S A* **117**, 12817–12825 (2020).
59. Ayad, N. M. E., Kaushik, S. & Weaver, V. M. Tissue mechanics, an important regulator of development and disease. *Philosophical Transactions of the Royal Society B: Biological Sciences* vol. 374 Preprint at https://doi.org/10.1098/rstb.2018.0215 (2019).
60. Bazellières, E. *et al.* Control of cell-cell forces and collective cell dynamics by the intercellular adhesome. *Nat Cell Biol* **17**, 409–420 (2015).
61. Palmquist, K. H. *et al.* Reciprocal cell-ECM dynamics generate supracellular fluidity underlying spontaneous follicle patterning. *Cell* **185**, 1960-1973.e11 (2022).

62. De Mets, R. *et al.* Cellular tension encodes local Src-dependent differential β1 and β3 integrin mobility. *Mol Biol Cell* **30**, 181–190 (2019).
63. Von Erlach, T. C., Hedegaard, M. A. B. & Stevens, M. M. High resolution Raman spectroscopy mapping of stem cell micropatterns. *Analyst* **140**, 1798–1803 (2015).
64. Pérez-González, C. *et al.* Active wetting of epithelial tissues. *Nat Phys* **15**, 79–88 (2019).
65. Wang, Y. C. The origin and the mechanism of mechanical polarity during epithelial folding. *Seminars in Cell and Developmental Biology* vol. 120 94–107 Preprint at https://doi.org/10.1016/j.semcdb.2021.05.027 (2021).
66. Sharrock, T. E. & Sanson, B. Cell sorting and morphogenesis in early Drosophila embryos. *Semin Cell Dev Biol* **107**, 147–160 (2020).
67. Chen, T., Saw, T. B., Mege, R. M. & Ladoux, B. Mechanical forces in cell monolayers. *J Cell Sci* **131**, (2018).
68. Yamada, S. & Nelson, W. J. Localized zones of Rho and Rac activities drive initiation and expansion of epithelial cell-cell adhesion. *Journal of Cell Biology* **178**, 517–527 (2007).

Figure 1

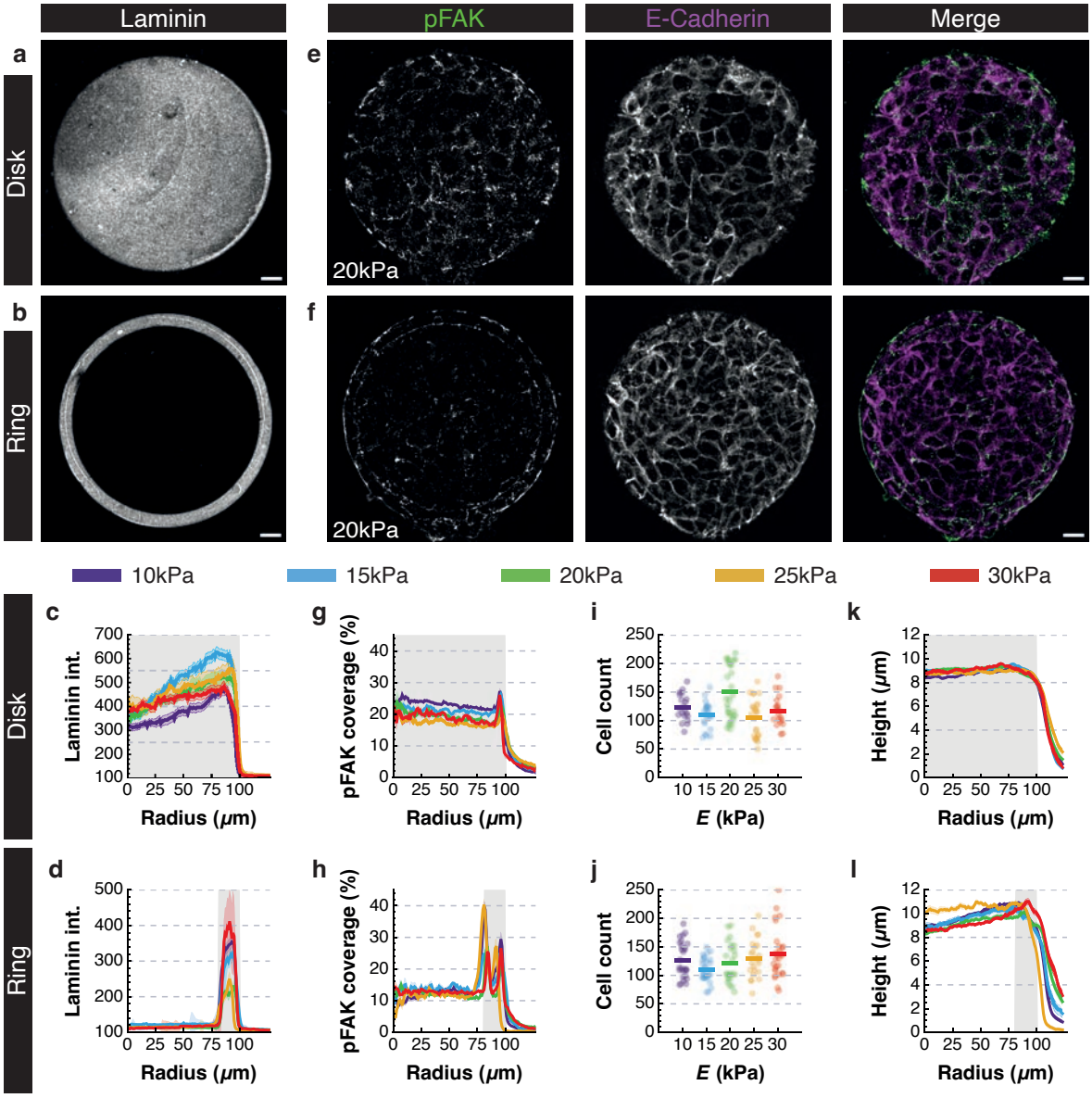
Laminin
pFAK
E-Cadherin
Merge
a
b
e
f
Disk
Ring
20kPa
20kPa
10kPa
15kPa
20kPa
25kPa
30kPa
c
d
g
h
i
j
k
l
Laminin int.
pFAK coverage (%)
Cell count
Height (μm)
Radius (μm)
E (kPa)

933 **Fig. 1. Modulating adhesive surface of EpH4 monolayers. a,b** Example projection of laminin
934 micropatterns for disk (**a**) and ring (**b**). **c,d** Quantification of mean laminin intensity radially
935 across micropatterns. **e,f** Example projections of basal pFAK and apical E-Cadherin on disk
936 (**e**) and ring (**f**) micropatterns. **g,h** Quantification of mean pFAK coverage radially across
937 micropatterns. **i,j** Dot plot of cell number within each monolayer, bars highlight mean value
938 for each population. **k,l** Quantification of mean cell height radially across micropatterns. For
939 all quantification thick line are mean values and ribbons are S.E.M, grey shaded region
940 represents adhesive surface. All N numbers and statistics included in Table S1 in
941 Supplementary Information. All scale bars = 20μm.
942
943
944

Figure 2

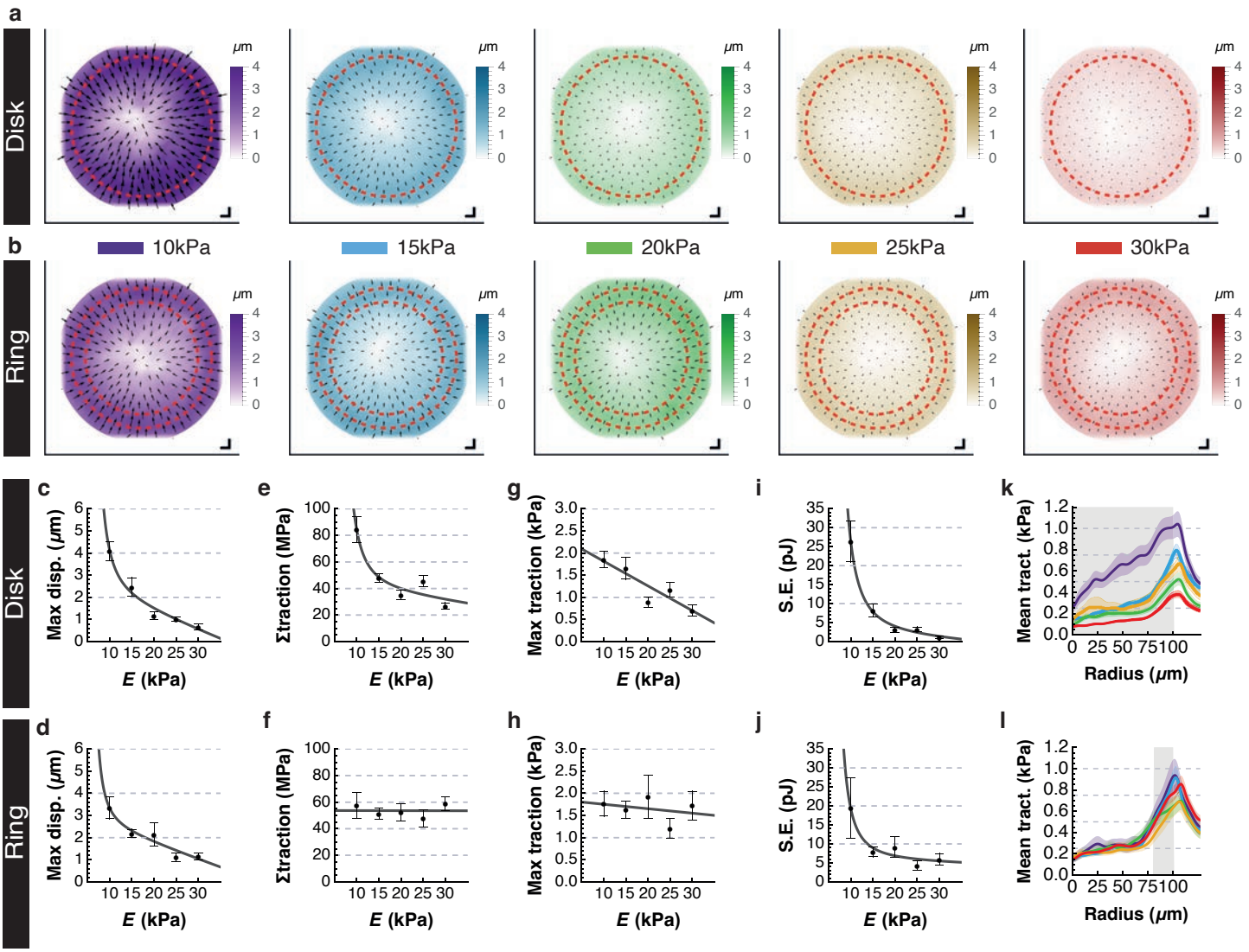
a
Disk
b
Ring
μm
10kPa
15kPa
20kPa
25kPa
30kPa
c
d
e
f
g
h
i
j
k
l
Max disp. (μm)
Σtraction (MPa)
Max traction (kPa)
S.E. (pJ)
Mean tract. (kPa)
E (kPa)
Radius (μm)

Fig. 2. Monolayer traction stresses are altered by modulating adhesive surface. a,b Mean displacement vector plots for monolayers on disks (**a**) and rings (**b**) on different substrate stiffnesses. Red dashed line outlines the adhesive surface and scale bars represent 4μm. **c,d** Quantification of maximum bead displacement by monolayers adhered to disks and rings on different substrate stiffnesses. **e,f** Quantification of total traction forces generated by monolayers adhered to disks and rings on different substrate stiffnesses. **g,h** Quantification of maximum traction forces generated by monolayers adhered to disks and rings on different substrate stiffnesses. **i,j** Quantification of strain energy transferred by monolayers into substrate adhered to disks and rings on different substrate stiffnesses. For **c-j** black dots highlight mean value, whiskers represent S.E.M and grey line is line of best fit. **k,l** Quantification of mean traction forces radially across micropatterns. Thick lines are mean values and ribbons are S.E.M, grey shaded region represents adhesive surface.

Figure 3

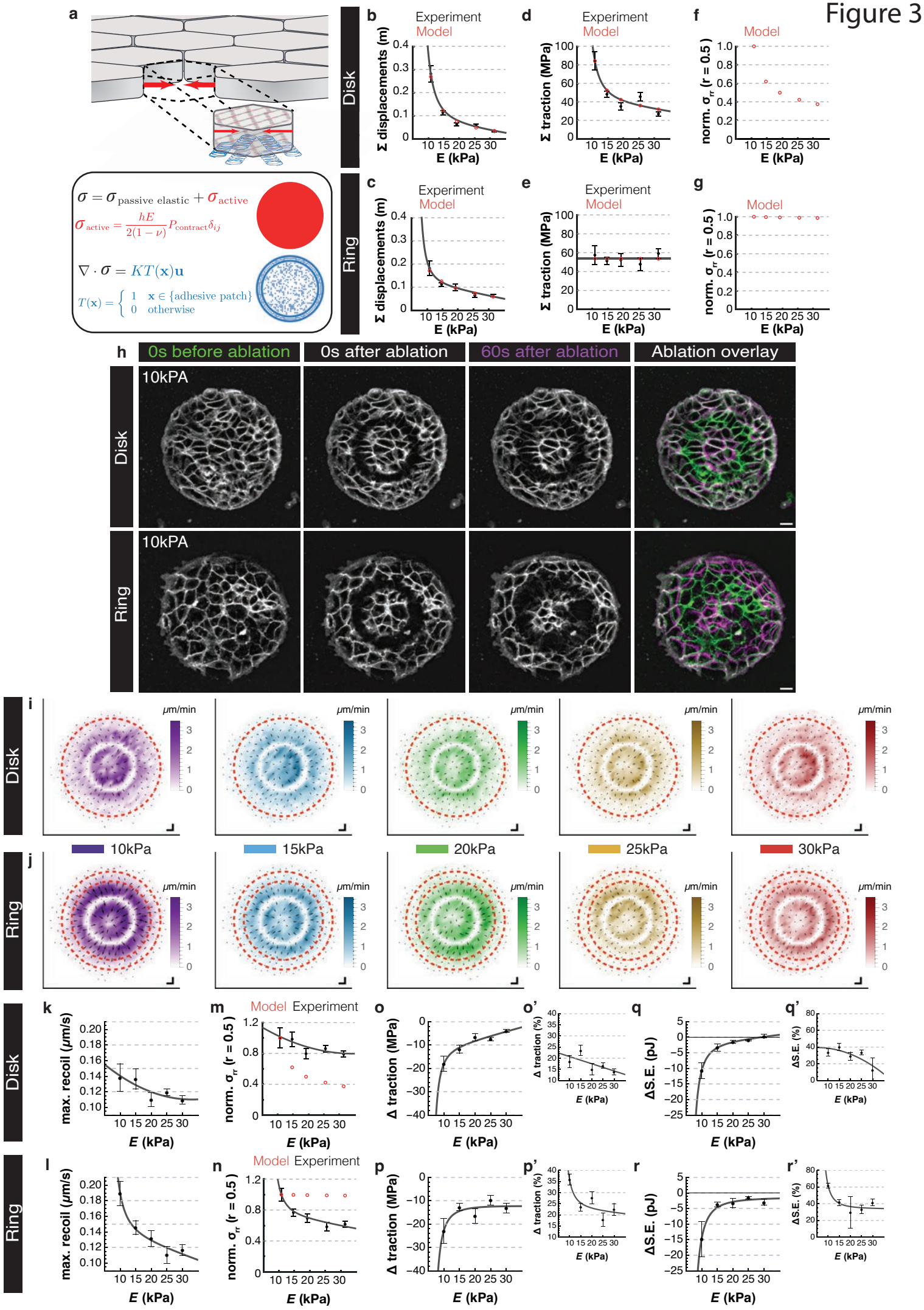
a
$\sigma = \sigma_{\text{passive elastic}} + \sigma_{\text{active}}$
$\sigma_{\text{active}} = \frac{hE}{2(1-\nu)} P_{\text{contract}} \delta_{ij}$
$\nabla \cdot \sigma = KT(\mathbf{x})\mathbf{u}$
$T(\mathbf{x}) = \begin{cases} 1 & \mathbf{x} \in \{\text{adhesive patch}\} \\ 0 & \text{otherwise} \end{cases}$
Disk
Ring
b
c
d
e
f
g
Experiment
Model
Σ displacements (m)
Σ traction (MPa)
norm. σ_{rr} (r = 0.5)
E (kPa)
h
0s before ablation
0s after ablation
60s after ablation
Ablation overlay
10kPA
i
j
μm/min
10kPa
15kPa
20kPa
25kPa
30kPa
k
l
m
n
o
p
o'
p'
q
r
q'
r'
max. recoil (μm/s)
Δ traction (MPa)
Δ traction (%)
ΔS.E. (pJ)
ΔS.E. (%)
E (kPa)

958 **Fig. 3. Intercellular stress is not proportional to traction stress. a** Schematic representation
959 of the major components that comprise the force balance model. Cells are considered as
960 active contractile agents (red arrows) bound together to form a monolayer continuum as
961 well as being bound to the substrate through adhesions (blue springs). Any stresses within
962 the monolayer are therefore a product of these active forces and passive elastic forces
963 transmitted through the monolayer (top equation). The active forces generated by the cells
964 are modelled as a pressure term (red equation) describing cell contractility, and for the
965 initial model we assumed a uniform distribution of contractility. Cell adhesions are
966 distributed throughout the monolayer based on experimental observations (blue
967 schematic), and at these points stresses within the monolayer are transmitted to the
968 substrate to deform it (bottom two equations). Schematic produced in part with
969 Biorender.com. **b,c** Total hydrogel displacement from experiments (same as Fig. S2g,h) were
970 used to parameterise the model. **d,e** Based on this parameterisation the model can
971 recapitulate the overall trend in experimental traction forces (same as Fig. 2e,f). **f,g** Model
972 predictions on intercellular stresses at the radial midpoint of the layer (r=0.5) normalised to
973 E=10kPa show changes as substrate stiffness increases. The model predicts intercellular
974 forces change in a manner similar to the total traction forces as substrate stiffness
975 increases. **h** Example time course projections of our laser ablation procedure for both
976 micropatterns. A ring ROI with outer radius of 50µm and inner radius of 40µm was ablated.
977 Merge shows overlay of 0s before and 60s after the ablation only to highlight deformations,
978 where white highlights regions of no deformation. Scale bar = 20µm. **i,j** Mean recoil velocity
979 vector plots for monolayers adhered on disks (**i**) and rings (**j**) on different substrate
980 stiffnesses. Red dashed line outlines the adhesive surface and scale bars represent
981 3.5µm/min. **k,l** Quantification of maximum recoil velocity after ablation for monolayers
982 adhered to disks and rings on different substrate stiffnesses. **m,n** Recoil velocity (same as
983 Fig. 3k,l) and model predictions of radial midpoint intercellular stresses (same as Fig. 3f,g)
984 have both been normalised to the value on the softest hydrogel (E=10kPa). The model is not
985 able to mimic experimental observations. **o-r** Quantification of the total loss in traction
986 forces (**o,p**) and strain energy (**q,r**) after ablations and once a new steady state is reached,
987 for monolayers adhered to disks (**o,q**) and rings (**p,r**) on different substrate stiffnesses.
988 Where **o'-r'** represent this value as a percentage of total traction forces (see Fig. 2e,f, **o',p'**)
989 and strain energy (see Fig. 2i,j, **q',r'**). For all quantification graphs, experimental data is in

black, with dots representing mean value, whiskers the S.E.M and grey line the line of best fit. Model outputs are red circles, where included.

Figure 4

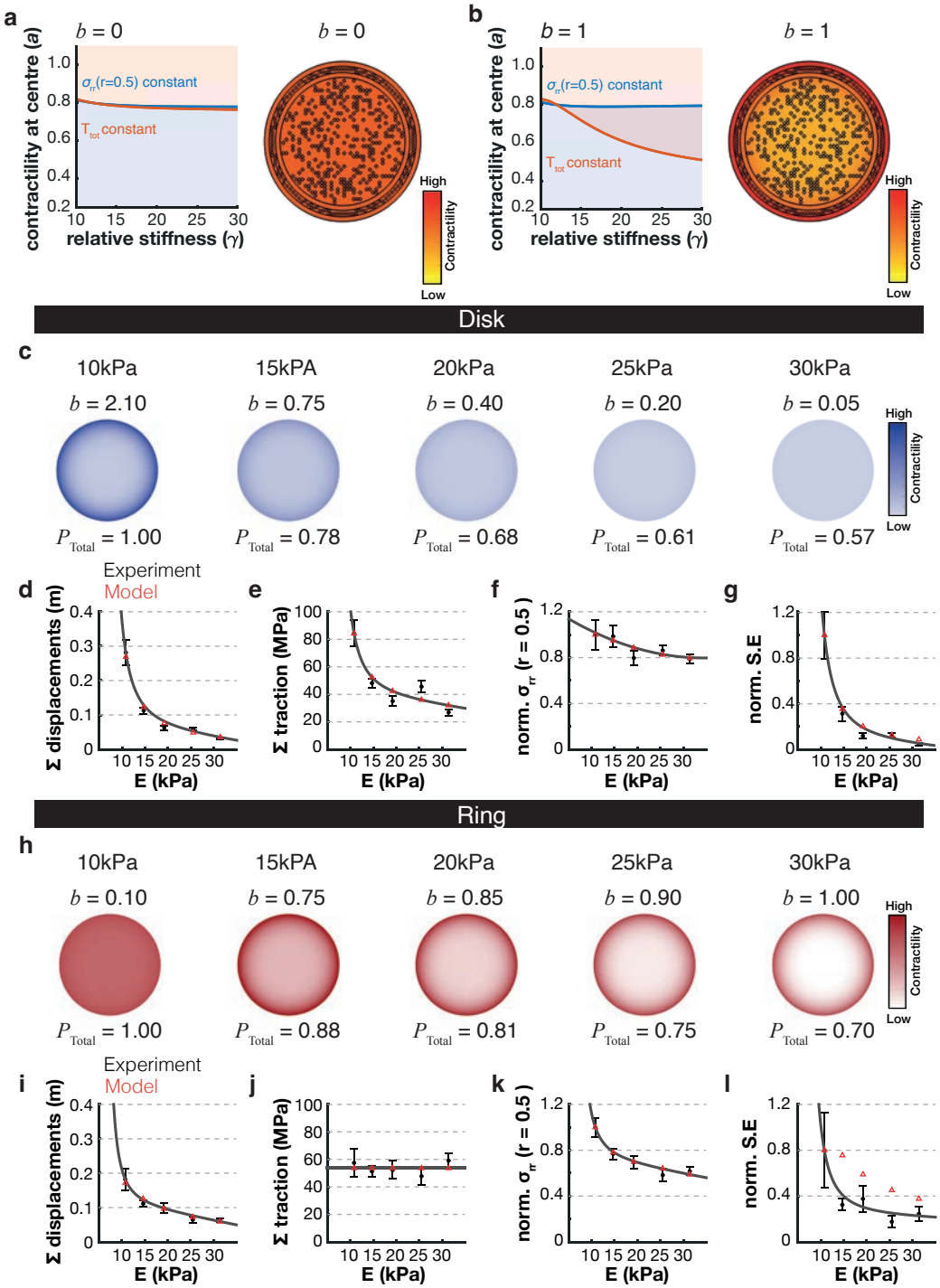
a
b = 0
b = 0
contractility at centre (a)
σrr(r=0.5) constant
Ttot constant
relative stiffness (γ)
High
Contractility
Low
b
b = 1
b = 1
contractility at centre (a)
σrr(r=0.5) constant
Ttot constant
relative stiffness (γ)
High
Contractility
Low
Disk
c
10kPa
15kPA
20kPa
25kPa
30kPa
b = 2.10
b = 0.75
b = 0.40
b = 0.20
b = 0.05
High
Contractility
Low
PTotal = 1.00
PTotal = 0.78
PTotal = 0.68
PTotal = 0.61
PTotal = 0.57
Experiment
Model
d
Σ displacements (m)
E (kPa)
e
Σ traction (MPa)
E (kPa)
f
norm. σrr (r = 0.5)
E (kPa)
g
norm. S.E
E (kPa)
Ring
h
10kPa
15kPA
20kPa
25kPa
30kPa
b = 0.10
b = 0.75
b = 0.85
b = 0.90
b = 1.00
High
Contractility
Low
PTotal = 1.00
PTotal = 0.88
PTotal = 0.81
PTotal = 0.75
PTotal = 0.70
Experiment
Model
i
Σ displacements (m)
E (kPa)
j
Σ traction (MPa)
E (kPa)
k
norm. σrr (r = 0.5)
E (kPa)
l
norm. S.E
E (kPa)

Fig. 4. Non-uniform contractility reconciles experimental observations. a,b Phase plane plots of contractility in the centre of the monolayer against substrate stiffness for ring monolayers only. The examples showcase situations where the spatial distribution of contractility (b), represented with accompanying heatmaps, is either uniform (b =0, **a**) or non-uniform (b =1, **b**). In both, solid lines represent situations where either intercellular stress at the radial midpoint of the layer (r=0.5) is constant (blue lines) or total traction forces generated by the monolayer is constant (red line). The shaded regions represent either situations where the intercellular stress must be lower (blue shaded region) or total traction forces must be greater (red shaded area). Note that on uniform contractility there is no workable overlap of shaded regions meaning no workable parameters exist that allow constant traction forces but lower intercellular stresses as substrate stiffness increases as occurs experimentally. However, with non-uniform contractility an overlap region does exist, highlighting a large parameter space which could reconcile experimental observations. For **c-l** the model was parameterised to include non-uniform contractility for both disks (**c-g**) and rings (**h-l**). **c,h** Schematic representations of the total and spatial distribution of contractility parameters (b = spatial distribution of contractility; P = total contractility normalised to softest substrate) used for disk (**c**) and rings (**h**) on different substrate stiffnesses. **d,i** Total hydrogel displacement from experiments (same as Fig. S2g,h), **e,j** total traction forces (same as Fig. 2e,f), and **f,k** normalised intercellular stress at the radial midpoint of the layer (r=0.5) normalised to the softest substrate (same as Fig. 3m,n) were used to parameterise the model. **g,l** Normalised strain energy to the softest substrate was used as a final check to examine the power of the model to mimic all experimental observations. Note that for disks (**g**) the model can reproducibly mimic experimental observations but for rings (**l**) it mimics the trend but does not reproduce the actual magnitude of change. For all quantification graphs, experimental data is in black, with dots representing mean value, whiskers the S.E.M and grey line the line of best fit and model outputs are red triangles.

Figure 5

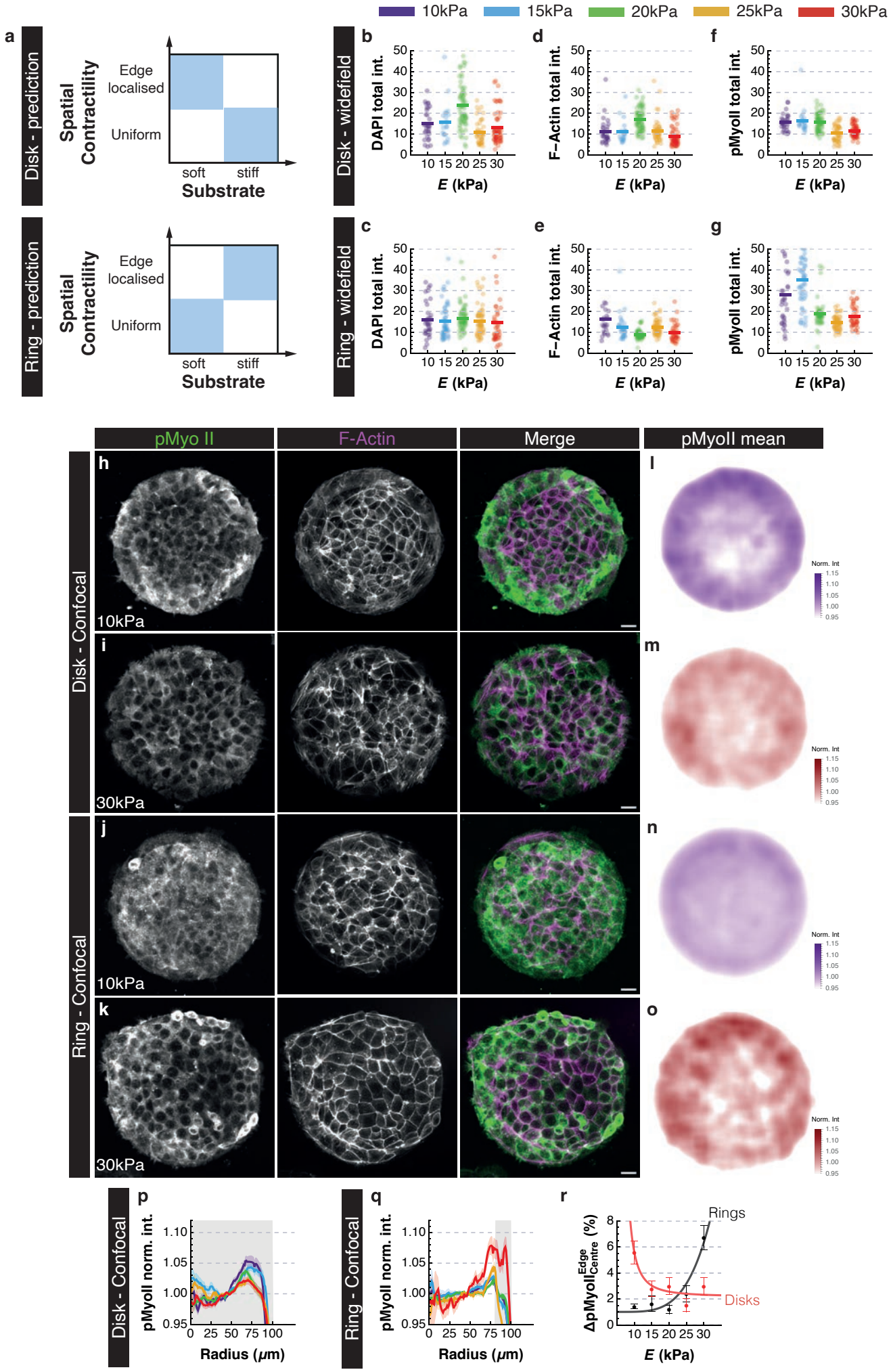
10kPa
15kPa
20kPa
25kPa
30kPa
a
Disk - prediction
Spatial Contractility
Edge localised
Uniform
soft
stiff
Substrate
Ring - prediction
Disk - widefield
Ring - widefield
b
c
d
e
f
g
DAPI total int.
F-Actin total int.
pMyoII total int.
E (kPa)
pMyo II
F-Actin
Merge
pMyoII mean
h
i
j
k
l
m
n
o
10kPa
30kPa
Norm. Int
Disk - Confocal
Ring - Confocal
p
q
r
pMyoII norm. int.
Radius (μm)
Rings
Disks
ΔpMyoII Edge/Centre (%)

1023 **Fig. 5. Contractility is non-uniform across micropatterned monolayers. a** Schematic
1024 representation of predictions based on parameterisation of the model. For disks the model
1025 suggests that there needs to be a shift in contractility from focused to the edge on soft
1026 substrates to more uniformity on stiffer substrates. On rings, the model suggests the
1027 opposite needs to occur with contractility being more uniform on soft substrates and
1028 becoming more localised to the edge on stiff substrates. **b-g** Dot plots of total intensity from
1029 widefield images within each monolayer for DAPI (**b,c**), F-Actin (**d,e**) and pMyoII (**f,g**)
1030 adhered to disks (**b,d,f**) and rings (**c,e,g**). Each dot represents one monolayer, and the bars
1031 represent mean value for each population. **h-k** Example projections of total monolayer
1032 intensity taken from confocal sections of pMyoII and F-Actin adhered to disk (**h,i**) and ring
1033 (**j,k**) micropatterns on soft (**h,j**) and stiff (**i,k**) hydrogels. Scale bar = 20µm. **l-o** Heatmaps of
1034 mean total monolayer pMyoII intensity normalised to the ablation ROI (40-50µm) for
1035 monolayers adhered to disks (**l,m**) and rings (**n,o**) on soft (**l,n**) and stiff (**m,o**) hydrogels. **p,q**
1036 Quantification of radial mean total pMyoII intensity normalised to the ablation ROI (40-
1037 50µm) for monolayers adhered to disks (**p**) and rings (**q**) on different substrate stiffnesses. **r**
1038 Quantification of percentage difference in normalised total monolayer pMyoII intensity
1039 between edge (>60µm) and centre (<40µm) radii. Dots represent mean value, whiskers
1040 S.E.M and shaded line the line of best fit, with disks in red and rings in black. Note that the
1041 trend corroborates the model predictions (**a**).
1042

Supplemental Figure 1

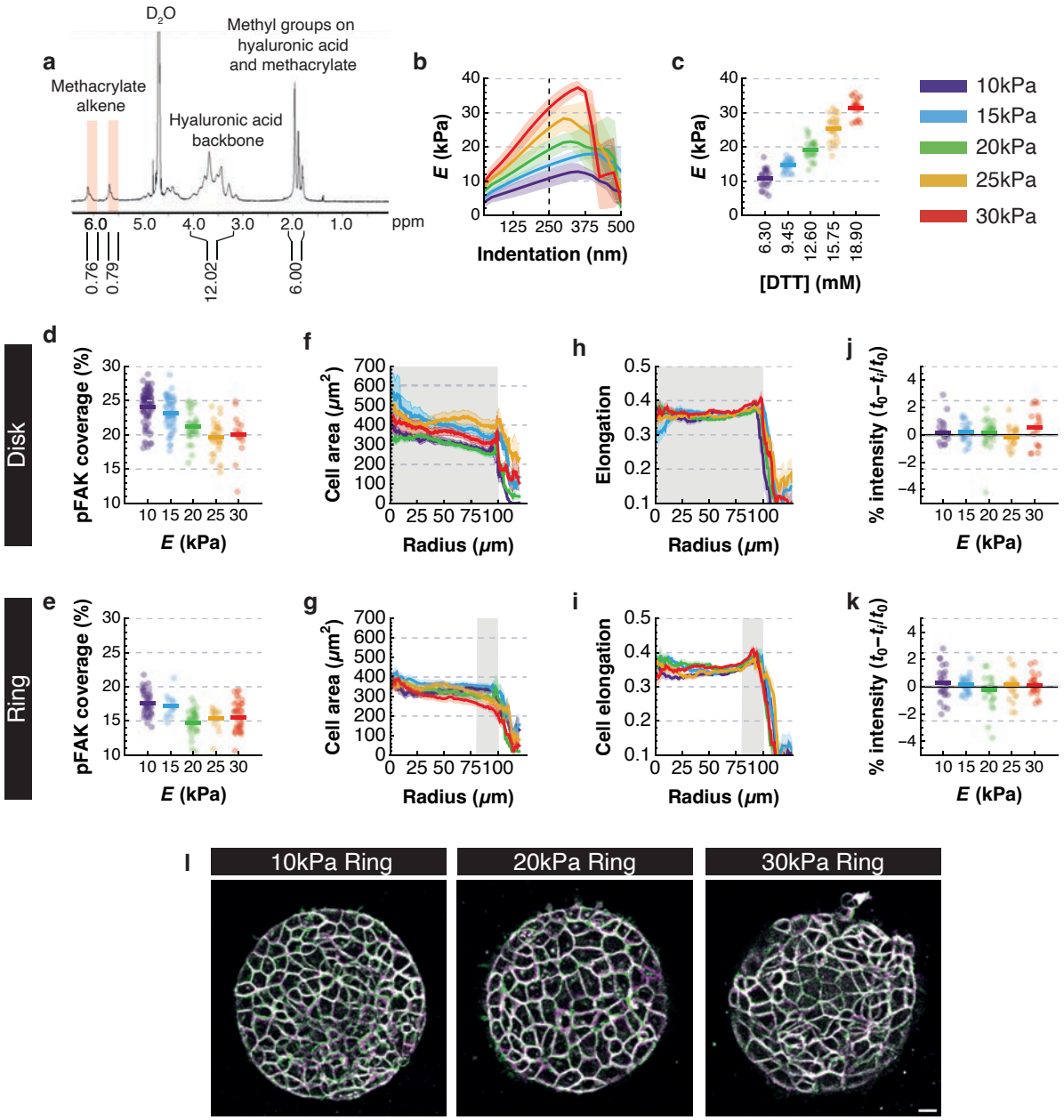

1043 **Fig. S1. Characterisation of micropatterned MeHA on EpH4 cells. a** ^{1}H NMR spectra of
1044 methacrylated hyaluronic acid (MeHA). **b** Young's moduli at different indentation depths on
1045 3%(w/v) MeHA hydrogels cross-linked with different DTT concentrations. Dashed line is at
1046 250nm which was used to define the Young's moduli for each DTT concentration. **c** Dot plot
1047 of Young's moduli for each concentration of DTT. Each dot is the average value from 50
1048 force-curves taken for a 100μm x 100μm region. **d,e** Dot plot of total pFAK coverage within
1049 each monolayer, bars highlight mean value for each population. **f,g** Quantification of mean
1050 cell area radially across micropatterns. **h,i** Quantification of mean cell elongation radially
1051 across micropatterns. For **f-i** thick line are mean values and ribbons are S.E.M, grey shaded
1052 region represents adhesive surface. **j,k** Dot plot of % intensity change after subtracting the
1053 cell outline projection from the frame before an annular ablation from the initial frame 1
1054 minute before. Lines represent mean value for each population. **l** Cell outline projections
1055 five minutes apart overlayed with the initial frame in green and last frame in Magenta.
1056 White represents pixels where there is no change in intensity. All N numbers and statistics
1057 included in Table S2 in Supplementary Information. All scale bars = 20μm.
1058
1059

Supplemental Figure 2

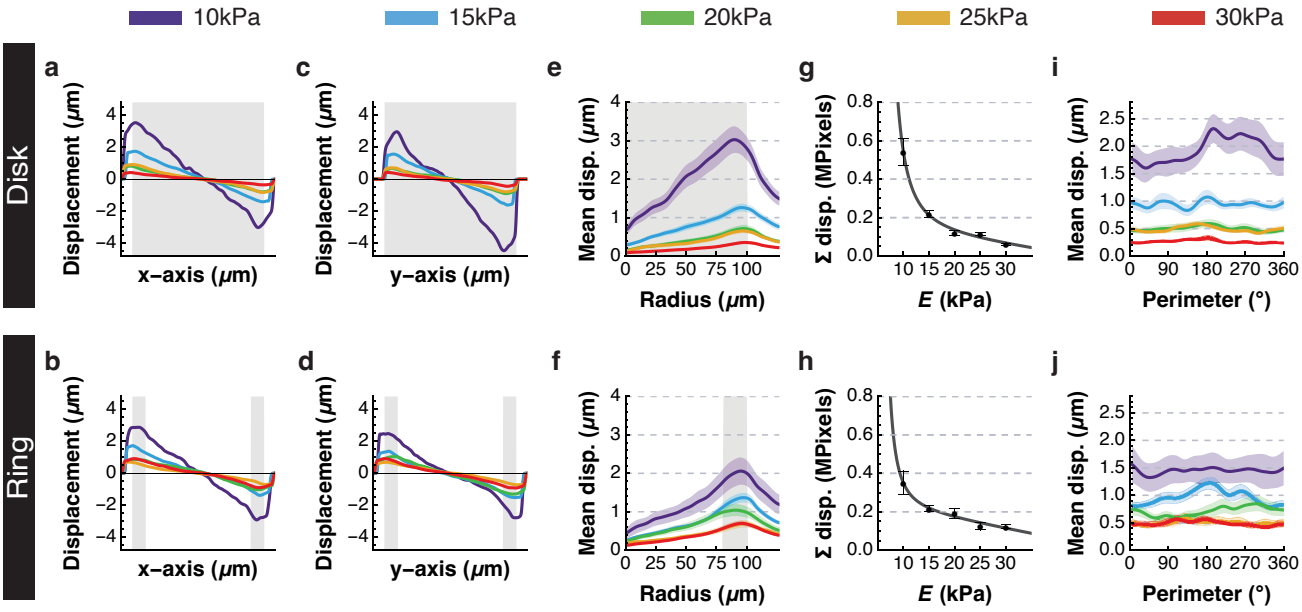

Fig. S2. Displacements of microbeads embedded within MeHA hydrogels by EpH4 monolayers. a-d Quantification of mean displacement along the x-axis (**a,b**) and y-axis (**c,d**). Grey region represents adhesive surface. **e,f** Quantification of mean displacement radially across micropatterns, where thick lines are mean values, ribbons are S.E.M, and grey shaded region represents adhesive surface. **g,h** Quantification of total bead displacements generated by monolayers adhered to disks and rings on different substrate stiffnesses. Dots represent mean values, whiskers are S.E.M, and grey line is line of best fit. **i,j** Quantification of the mean bead displacement around the perimeter of monolayers, with 0° along the horizontal axis, where thick lines are mean values, ribbons are S.E.M, and grey shaded region represents adhesive surface.

Supplemental Figure 3

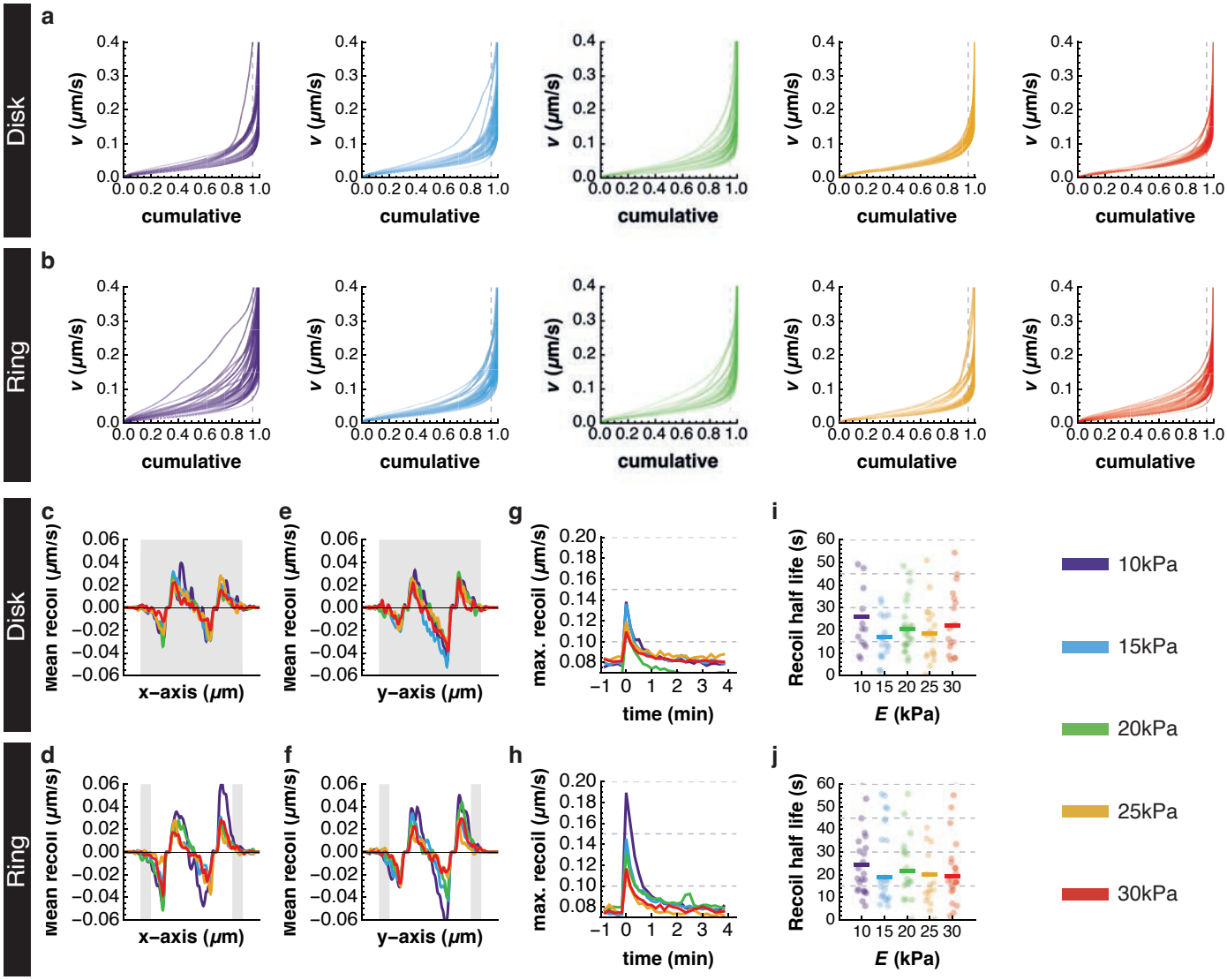

Fig. S3. Recoil velocity dynamics and correlations after laser ablation. a,b Cumulative plots of all recoil velocity values for each movie on both micropatterns. To calculate the maximum recoil value the 95th percentile (grey dashed line) value was used, which was always located near the edge of the ablation site. **c-f** Quantification of mean recoil velocity along the x-axis (**c,d**) and y-axis (**e,f**). Grey region represents adhesive surface. **g,h** Quantification of the mean maximum recoil velocity over the time course of our movies for both micropatterns. **i,j** Dot plot of recoil half-life calculated from Fig. S3g,h. Each dot represents a movie, and the line represents population mean value.

Supplemental Figure 4

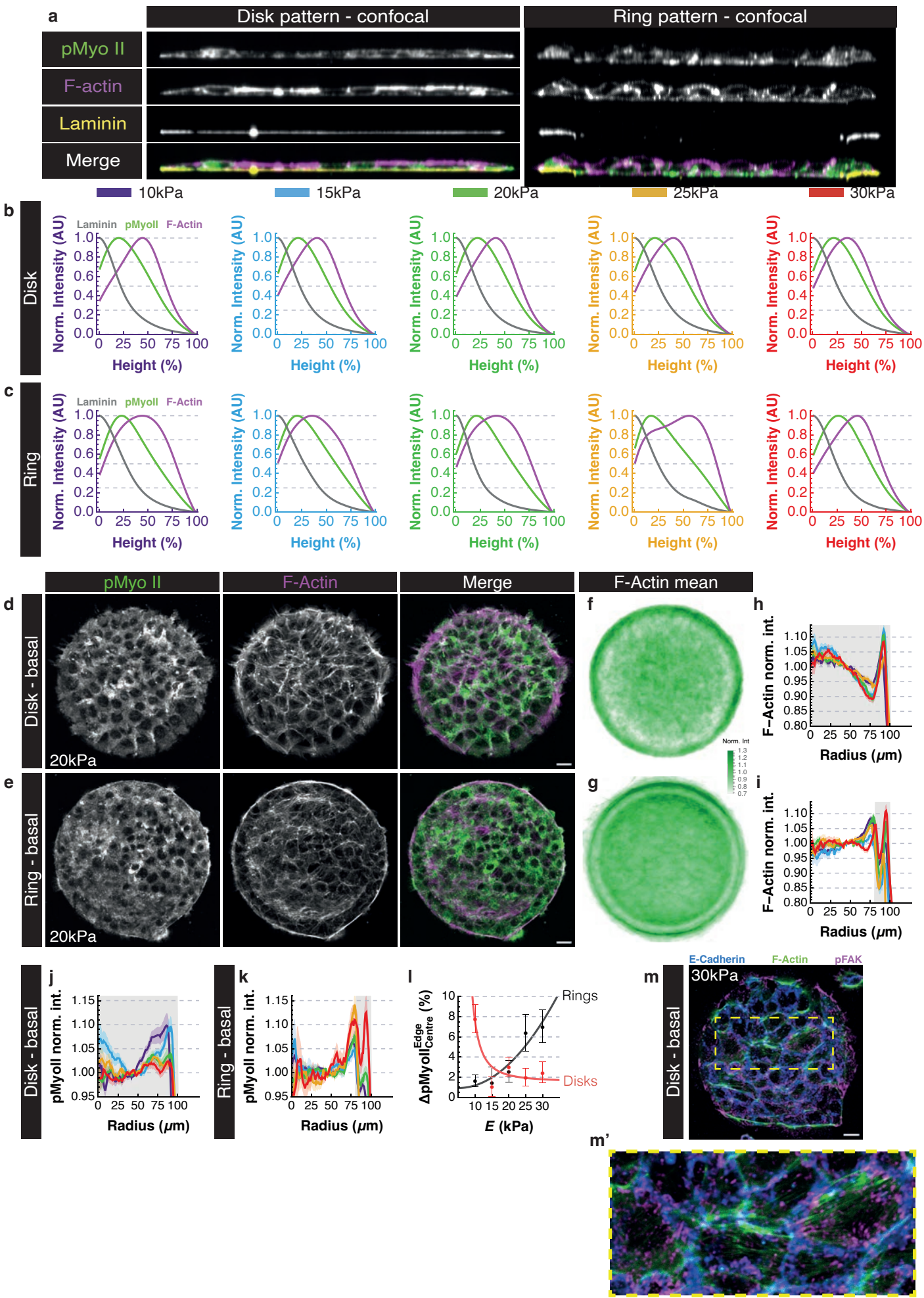

1082 **Fig. S4. pMyoII localisation within monolayers. a** Example orthogonal projections through
1083 the middle of a monolayer of pMyoII, F-Actin and Laminin on disk (left) and ring (right)
1084 micropatterns. **b,c** Quantification of mean orthogonal intensity of laminin, pMyoII and F-
1085 Actin normalised to the maximum value for the entire orthogonal projection (see **a**). Note
1086 that pMyoII maximum intensity is always near the laminin intensity highlighting basal
1087 accumulation of pMyoII, whilst F-actin peak is close to 50% of cell height where cell-cell
1088 junctions are located. **d,e** Example projections of basal monolayer intensity taken from
1089 confocal sections of pMyoII and F-Actin adhered to disk (**d**) and ring (**e**) micropatterns on
1090 20kPa hydrogels. **f,g** Heatmaps of mean F-Actin intensity from basal projections normalised
1091 to the ablation ROI (40-50μm) for monolayers adhered to disks (**f**) and rings (**g**) on 20kPa
1092 hydrogels. **h,i** Quantification of radial mean F-Actin intensity from basal projections
1093 normalised to the ablation ROI (40-50μm) for monolayers adhered to disks (**h**) and rings (**i**)
1094 on different substrate stiffnesses. **j,k** Quantification of radial mean pMyoII intensity from
1095 basal projections normalised to the ablation ROI (40-50μm) for monolayers adhered to disks
1096 (**j**) and rings (**k**) on different substrate stiffnesses. For **h-k**, thick lines are mean values,
1097 ribbons are S.E.M, and grey shaded region represents adhesive surface. **l** Quantification of
1098 percentage difference in normalised pMyoII intensity from basal projections between edge
1099 (>60μm) and centre (<40μm) radii. Dots represent mean value, whiskers S.E.M and shaded
1100 line the line of best fit, with disks in red and rings in black. Note a similar trend to total
1101 projections seen in Fig. 5r). **m** Example basal projection of pFAK, F-Actin and E-Cadherin on
1102 disk micropattern with expanded insert (**m'**) to highlight F-Actin fibres that span epithelial
1103 cells, mainly between pFAK labelled adhesions. Scale bar = 20μm.